

Unveiling the nature of SN 2022jli: the first double-peaked stripped-envelope supernova showing periodic undulations and dust emission at late times

Régis Cartier^{1,2*}, Carlos Contreras³, Maximilian Stritzinger⁴, Mario Hamuy^{5,6}, Pilar Ruiz-Lapuente^{7,8},
Jose L. Prieto², Joseph P. Anderson⁹, Aleksandar Cikota¹, and Matthias Gerlach^{1,2,10}

¹ Gemini Observatory, NSF's National Optical-Infrared Astronomy Research Laboratory, Casilla 603, La Serena, Chile

² Instituto de Estudios Astrofísicos, Facultad de Ingeniería y Ciencias, Universidad Diego Portales, Av. Ejército Libertador 441, Santiago, Chile

³ Las Campanas Observatory, Carnegie Observatories, Casilla 601, La Serena, Chile

⁴ Department of Physics and Astronomy, Aarhus University, Ny Munkegade 120, DK-8000 Aarhus C, Denmark

⁵ Fundación Chilena de Astronomía, Santiago, Chile

⁶ Hagler Institute for Advanced Studies, Texas A&M University, Texas, USA

⁷ Instituto de Física Fundamental, Consejo Superior de Investigaciones Científicas, c/. Serrano 121, E-28006, Madrid, Spain

⁸ Institut de Ciències del Cosmos (UB-IEEC), c/. Martí i Franqués 1, E-080228, Barcelona, Spain

⁹ European Southern Observatory, Alonso de Córdova 3107, Casilla 19, Santiago, Chile

¹⁰ Instituto de Astrofísica, Facultad de Física, Pontificia Universidad Católica de Chile, Av. Vicuña Mackenna 4860, Santiago, Chile

Received ; accepted

ABSTRACT

We present optical and infrared observations from maximum light until around +600 days of supernova (SN) 2022jli, a peculiar stripped envelope (SE) SN showing two maxima, each one with a peak luminosity of about $3 \times 10^{42} \text{ erg s}^{-1}$ and separated by fifty days. The second maximum is followed by unprecedented periodic undulations with a period of $P \sim 12.5$ days. The spectra and the photometric evolution of the first maximum are consistent with the behaviour of a standard SE SN with an ejecta mass of $1.5 \pm 0.4 M_{\odot}$, and a radioactive ^{56}Ni mass of $0.12 \pm 0.01 M_{\odot}$. The optical spectra after +400 days relative to the first maximum correspond to a standard SN Ic event, and at late times SN 2022jli exhibits a significant drop in the optical luminosity implying that the physical phenomena that produced the secondary maximum has ceased to power the SN light curve. One possibility is that the secondary maximum is powered by a magnetar with an initial spin period of $P = 48.5$ ms and a high magnetic field of $B = 8.5 \times 10^{14}$ G, while the light curve periodic undulations could be produced by accretion of material from a companion star onto the neutron star in a binary system. The near-infrared spectra shows clear 1st CO overtone emission from about +190 days after the first maximum, and it becomes undetected at +400 days. A significant near-infrared excess from hot dust emission is detected at +238 days produced by either newly formed dust in the SN ejecta or due to a strong near-infrared dust echo. Depending on the assumptions of the dust composition, the estimated dust mass is $2 - 16 \times 10^{-4} M_{\odot}$. The magnetar power of the second maximum can fit in a more general picture where magnetars are the power source of super-luminous SNe, could produce their frequent bumps and undulations, and where pulsars could produce the late time excess observed in some SE SNe. The detection of CO and the potential detection of dust formed in the ejecta of SN 2022jli are important to understand the formation molecules and dust in the ejecta of SE SNe.

Key words. supernova: general - supernova: individual: SN 2022jli

1. Introduction

Massive stars with zero-age main-sequence (ZAMS) masses larger than $\approx 10 M_{\odot}$ end their lives as core-collapse supernovae (SNe), giving birth to neutron stars and black holes. These stellar explosions can be broadly divided in hydrogen-rich Type II SNe exhibiting strong and long-lasting hydrogen features in their spectra, and hydrogen-deficient stripped-envelope (SE) SNe which have lost the majority of their hydrogen and helium envelopes over their evolutionary lifetimes (see Filippenko 1997; Gal-Yam 2017).

A scenario initially proposed for SE SNe was the explosion of single massive Wolf-Rayet (WR) stars that have lost their envelopes through strong winds (Conti 1975). In this scenario, SE SNe (I Ib, I b and Ic) follow a sequence in mass, where the most

massive stars suffer from stronger winds losing a larger fraction of their envelopes before demise as a SN event. This predicts that the most massive stars demise as SNe Ic losing all of their hydrogen and most, if not all, of their helium envelopes.

An alternative progenitor scenario for SE SNe are massive stars in binary systems that shed much of their envelopes through binary interaction (Podsiadlowski et al. 1992), while in the late-stage of their evolution, stellar winds can play a key role in peeling off the remaining hydrogen (Ib's) and helium (Ic's) in their outermost layers (see e.g., Yoon 2017; Dessart et al. 2020). This scenario allows a larger range of initial stellar masses to become SE SNe, but still the most massive stars lose a larger fraction of their envelopes and explode as SNe Ic (Yoon 2017; Dessart et al. 2020). This scenario is supported by the large fraction of young massive stars in binary systems (Sana et al. 2012), and by their small ejecta masses (M_{ej}) ranging between about $1 - 5 M_{\odot}$ (Drout

* rgcartier@gmail.com

et al. 2011; Cano 2013; Taddia et al. 2015; Lyman et al. 2016; Prentice et al. 2016; Taddia et al. 2018b), which are too small to be consistent with single massive stars. Their radioactive ^{56}Ni mass (M_{Ni}) is in the range of $0.05 - 0.3 M_{\odot}$ from sample studies of SE SNe (Drout et al. 2011; Cano 2013; Taddia et al. 2015; Lyman et al. 2016; Prentice et al. 2016; Taddia et al. 2018b; Anderson 2019).

Standard SE SNe display bell-shaped light curves having a single maximum (see e.g., Taddia et al. 2015, 2018a),¹ powered by the decay of radioactive ^{56}Ni . SN 2005bf (Monard et al. 2005) was the first SE SN reported to show a peculiar light curve morphology composed of two maxima separated by about 25 days (Anupama et al. 2005; Tomimaga et al. 2005; Folatelli et al. 2006; Maeda et al. 2007; Stritzinger et al. 2018b). The canonical radioactive decay of ^{56}Ni distributed close to the SN center is not able to produce bumpy or double-peaked light curves. However, a double-peaked distribution of radioactive ^{56}Ni , with an enhanced ^{56}Ni abundance near the SN surface, provides a reasonable alternative to produce double-peaked light curves (see Orellana & Bersten 2022, for a discussion). This was the first scenario proposed to explain the light curves of SN 2005bf (Tomimaga et al. 2005; Folatelli et al. 2006), however it faces the difficulty to reconcile the relatively high ^{56}Ni mass predicted with the fast decline and the faint SN luminosity at about a year after the explosion (see Maeda et al. 2007). Motivated by this discrepancy, Maeda et al. (2007) proposed that the energy injection from a newly born magnetar could explain the maximum light morphology, the rapid decline and the faint luminosity of SN 2005bf at late times. Since then, PTF11mnb (Taddia et al. 2018a) and SN 2019cad (Gutiérrez et al. 2021) are two SE SNe reported to display similar light curves morphology to SN 2005bf. In both cases their light curves can be modelled with a double-peaked distribution of ^{56}Ni . Gutiérrez et al. (2021) show that the light curves of SN 2019cad can be equally modelled with a central distribution of ^{56}Ni and power injection from a magnetar, which powers the second maximum. Another noteworthy event is SN 2022xxf (Itagaki 2022). This SN was discovered before maximum and promptly classified as a SN Ic broad line (Ic-BL; Balcon 2022). It shows two prominent maxima separated by 75 days, the second maximum reached a slightly brighter luminosity and bluer colours, compared with the first maximum (Kuncarayakti et al. 2023). The first maximum seems to correspond to a standard SN Ic-BL event, while the second maximum has been argued to be powered by the interaction between the SN ejecta with a massive (a few M_{\odot}) hydrogen and helium poor circum-stellar medium (CSM; see Kuncarayakti et al. 2023). This hypothesis is based on spectral features suggesting ejecta-CSM interaction and on the appearance of a conspicuous intermediate width line component (FWHM $\sim 2500 \text{ km s}^{-1}$) on top of the broad emission (FWHM $\sim 5000 \text{ km s}^{-1}$). The spectral evolution is slow and after the second maximum the light curve declines rapidly.

Hydrogen-deficient super-luminous SE SNe (SLSNe-Ic) correspond to a luminous class of objects encompassing peak luminosities from $\sim 10^{43} \text{ erg s}^{-1}$ or -20 mag (see e.g., De Cia et al. 2018; Lunnan et al. 2018; Angus et al. 2019) to $\sim 3 \times 10^{44} \text{ erg s}^{-1}$ or -22.5 mag (see e.g., De Cia et al. 2018; Lunnan et al. 2018; Angus et al. 2019; Cartier et al. 2022). Their large peak luminosities are difficult to produce through standard SN powering mech-

anisms such as the canonical decay of ^{56}Ni synthesized in the SN explosion. The most popular scenarios to explain the light curves of SLSNe-Ic are the power injection from a magnetar (Kasen & Bildsten 2010; Woosley 2010; Inserra et al. 2013), or strong interaction with hydrogen and helium poor CSM (see e.g., Chatzopoulos et al. 2013; Sorokina et al. 2016; Moriya et al. 2018, for a discussion). Pre-maximum bumps are often found in the light curves of the SLSNe-Ic population (Leloudas et al. 2012; Nicholl et al. 2015; Smith et al. 2016; Nicholl & Smartt 2016; Angus et al. 2019). These early bumps are usually explained by the shock cooling emission from extended material surrounding the progenitor star (see Nicholl & Smartt 2016; Piro 2015; Piro et al. 2021). Subsequent bumps, humps and light curve undulations are frequently found throughout SLSNe-Ic light curve evolution (Yan et al. 2015; Nicholl et al. 2016b; Yan et al. 2017; Hosseinzadeh et al. 2022; Cartier et al. 2022; Gutiérrez et al. 2022). Some bumps are likely explained by the interaction between the SN ejecta with a dense CSM (Yan et al. 2015, 2017), while in other cases they can be explained by the variable power injection from a magnetar (see Moriya et al. 2022).

A combination of mechanisms such as the decay of radioactive nickel, power injection from a magnetar and interaction between the SN ejecta with a dense CSM are invoked to explain the double-peaked light curve of the luminous SN 2019stc (Gomez et al. 2021). Early bumps can also be the result of the collision between the SN ejecta and a companion star, yielding double-peaked light curves (Kasen 2010), the result of magnetar driven shock-break out (Kasen et al. 2016), or the collision of the newborn neutron star with the companion star in a binary system (see Hirai & Podsiadlowski 2022).

SN 2022jli is a SE SN discovered near maximum light in the nearby galaxy NGC 157. SN 2022jli shows a strong secondary maximum followed by periodic or quasi-periodic undulations (Moore et al. 2023; Chen et al. 2024). Chen et al. (2024) proposed that the first maximum corresponds to a SE SN, and the second maximum and the subsequent light curve undulations are produced by the accretion from a companion star onto a compact object at periastron encounters in a binary system (see also King & Lasota 2024). Alternatively, Moore et al. (2023) proposed that the second maximum corresponds to a massive $12 \pm 6 M_{\odot}$ SN ejecta powered by the radioactive decay of ^{56}Ni , and the periodic variability could a consequence of ejecta-CSM interaction with the CSM configured in nested shells or due to the collision of a neutron star with the companion star as in the model of Hirai & Podsiadlowski (2022).

This work is structured as follows. In Section 2 we present optical and near-infrared (NIR) observations of SN 2022jli from maximum light to +600 days. In Section 3 we present the analysis of the observations of SN 2022jli, we estimate the host galaxy reddening in the line-of-sight, we present and analyse the bolometric light curve of SN 2022jli. We show that the SN is characterized by two maxima of similar luminosity, where the first maximum corresponds to a standard SN Ic, we estimate the SN ejecta mass and the ^{56}Ni mass under the assumption that the first maximum is powered by the radioactive decay of ^{56}Ni . We confirm the undulations in the optical light curves that appear after the second maximum, finding a period of about 12.5 days, consistent with Moore et al. (2023) and Chen et al. (2024). We study the spectral sequence starting from +12 days to +428 days, showing that during the secondary maximum the optical and NIR spectral features evolve slowly, implying that the SN ejecta remains heated by more than 150 days. At late times ($> +250$ days) the SN suffers a drop in luminosity reaching a luminosity comparable to a standard SE SN at about +400 days,

¹ Some SE SNe exhibit an early bump a few days after the explosion and several days before the ^{56}Ni powered maximum (eg., SN 1993J; see Richmond et al. 1994). This early excess emission is explained by shock cooling of extended material.

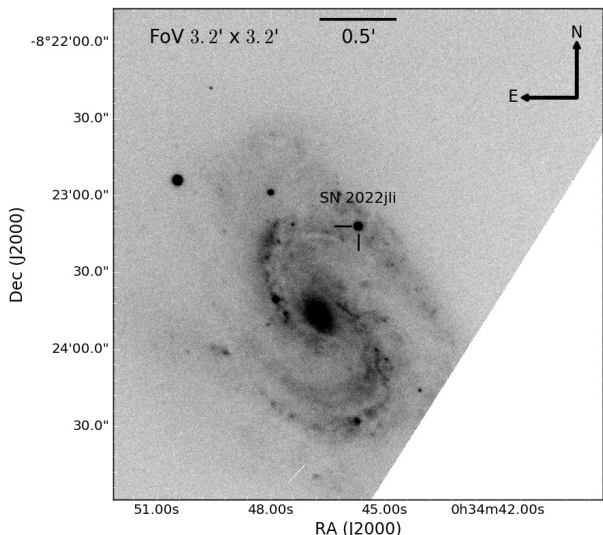


Fig. 1. Field of SN 2022jli in the *i*-band observed with the LDSS-3 mounted at the Baade telescope at Las Campanas Observatory on May 22nd, 2022. The position of the SN is indicated in the figure, north is up and east is to the left.

and the optical spectra after +400 days are typical of a SN Ic at nebular phase. We report the formation of carbon monoxide (CO) from the detection of the 1st CO overtone in the NIR spectra at +190 days and the emission of hot dust at late times (> +200 days) detected by means of a clear infrared excess. In Section 4, we discuss the super-Eddington accretion scenario (Chen et al. 2024; King & Lasota 2024) and the SN ejecta-CSM interaction scenario (Moore et al. 2023), and propose an alternative scenario in which in addition to the accretion of material from a companion star onto the neutron star, the power from the spin-down rotational energy from a magnetar contribute to power the second maximum. This alternative scenario alleviates the need of an extreme beaming to explain the high luminosity observed during the second maximum, and can be placed within the broad picture of bumps and undulations observed in magnetar powered SLSNe and late time excess potentially produced by pulsars in some SE SNe (see e.g., Ravi et al. 2023). In Section 5 we summarise our conclusions.

2. Observations and Data Reduction

SN 2022jli was discovered on 2022 May 05.17 UT by Libert Monard (Monard 2022) at an unfiltered (clear filter) apparent magnitude of 14.4 mag, which was later corrected to 14.22 ± 0.15 mag and reported to the Transient Name Server (TNS). The SN is located in the galaxy NGC 157 at equatorial coordinates of $\alpha = 00 : 34 : 45.7$ and $\delta = -08 : 23 : 12.07$ (J2000), in the northern spiral arm of its host galaxy, at $16''.2$ west and $35''.09$ north of the galaxy centre (see Fig. 1). SN 2022jli was classified as a SN Ic at a phase of one to three days after maximum based on a spectrum obtained on 2022 May 11.14 UT by Grzegorzek (2022), and later confirmed as a SN Ic by ePESSTO+ (Cosentino et al. 2022) based on a spectrum obtained on 2022 May 24.42 UT. Due to some confusion on the SN coordinates reported to TNS, the ePESSTO+ classification was erroneously reported as a separate object named SN 2022jzy.

2.1. Photometry

We analyse public optical photometry from the Kleinkaroo Observatory reported by Monard to the TNS, from the Gaia mission² (Gaia Collaboration et al. 2016), from the ATLAS survey (Tonry et al. 2018; Smith et al. 2020), from the Zwicky Transient Facility (ZTF; Bellm et al. 2019), and from All-Sky Automated Survey for Supernovae (ASAS-SN; Shappee et al. 2014). We also present optical photometry obtained with the LDSS-3 instrument mounted to the 6.5-m Magellan Clay telescope, the EFOSC2 instrument with the 3.58-m New Technology Telescope (NTT), the Goodman instrument mounted on the 4.1 m SOAR telescope, and NIR photometry obtained with the Flamingos-2 instrument on the 8.4-m Gemini-South observatory. The optical photometry extends from a few days before maximum light to +418 days after maximum, and the NIR photometry extends from +38 days to +600 days.

2.1.1. Optical

To discount any potential issue in the public ZTF photometry of SN 2022jli we downloaded the original ZTF images from the NASA/IPAC Infrared Science Archive,³ and performed host-galaxy template image subtraction using HOTPANTS (Becker 2015). Aperture and PSF photometry was then computed from these template subtracted science images using PYTHON scripts. ATLAS forced photometry from the ATLAS forced photometry server was also downloaded and included in our analysis.⁴ We include *g*-band ASAN-SN photometry to complement the photometry during the decline from the first maximum and on the rise to the second maximum. The ASAN-SN photometry correspond to photometry published by Moore et al. (2023) and Chen et al. (2024).

The reduction of the LDSS-3 and Goodman images was performed in IRAF following standard procedures that include bias subtraction and the normalization of the science images using a normalized flat image, the astrometric registration of the images was done using ASTROMETRY.NET (Lang et al. 2010). The reduction of the EFOSC2 *V*-band acquisition image was done with the PESSTO pipeline (Smartt et al. 2015). Aperture and PSF photometry was performed with PYTHON scripts (see e.g., Hueichapan et al. 2022). The optical photometry of SN 2022jli is presented in Fig. 2.

2.1.2. Near-infrared

NIR photometry of SN 2022jli was obtained using the Flamingos-2 instrument (Eikenberry et al. 2004, 2012) mounted on the Gemini-South telescope. Flamingos-2 images were reduced using custom IRAF scripts. The reduction steps include the creation of a clean sky image, and the subtraction of this image from the science frames, flat fielding the science frames and the astrometric registration of the science images using ASTROMETRY.NET (Lang et al. 2010). The sky images were created from frames obtained in a position far from the host galaxy to avoid over subtraction of the host galaxy emission in the sky subtraction process. The pre-explosion images of NGC 157 in *JHK_s*, obtained with the VIRCAM instrument (Dalton et al. 2006) mounted on the VISTA telescope (Emerson et al. 2006) at Paranal observatory were employed to subtract the host galaxy

² <http://gsaweb.ast.cam.ac.uk/alerts/alert/Gaia22cbu/>

³ <https://irsa.ipac.caltech.edu/Missions/ztf.html>

⁴ <https://fallingstar-data.com/forcedphot/>

background emission from the SN images. The NIR photometry of SN 2022jli is reported in Table 1 and shown in Fig. 2.

2.1.3. Mid-infrared

The field of the SN has been repeatedly visited by the Wide-field Infrared Survey Explorer (WISE) satellite (Wright et al. 2010) as part of the NEOWISE (Mainzer et al. 2011) and NEOWISE-R (Mainzer et al. 2014) missions. The NEOWISE-R mission observed the SN field four times during 2022 and 2023, after the SN explosion. A careful inspection of the NEOWISE-R images before and after the SN explosion shows a clear mid-IR emission from the SN in the *W1* and *W2* bands, and no variability pre-SN explosion, therefore we used pre-explosion images to subtract the host galaxy background emission from the images containing the SN. In each NEOWISE-R visit to a field of the order of 12 short exposures are typically obtained in a time span of a day. To obtain deep photometry we proceeded to co-add single exposure images obtained within a visit. A similar procedure was performed on the pre-SN images to obtain deep host galaxy templates. We obtained aperture photometry from most subtracted images. The NEOWISE *W1* and *W2* photometry is presented in Fig. 2 and summarised in Table 2.

2.2. Spectroscopy

2.2.1. Optical

We obtained optical spectra of SN 2022jli with the LDSS-3 spectrograph mounted at the Clay telescope at Las Campanas Observatory, the Goodman spectrograph (Clemens et al. 2004) mounted at the SOAR telescope and the GMOS-S spectrograph (Hook et al. 2004; Gimeno et al. 2016) at the Gemini-South telescope. The LDSS-3 and Goodman data were reduced using IRAF routines. The reduction steps include bias subtraction, flat fielding, cosmic ray rejection using LACosMIC (van Dokkum 2001), wavelength calibration, flux calibration and telluric correction. We performed the flux calibration and the telluric correction using a flux standard star observed on the same night of the SN spectra.

The GMOS-S spectra were reduced using the GEMINI IRAF package following standard reduction procedures similar to the ones described for the LDSS-3 and Goodman instruments, in this case using the gmos IRAF task. For the GMOS-S spectra, the wavelength calibration was performed using CuAr comparison lamps. The flux calibration was performed using a spectrophotometric standard star observed on a different night but with the same instrument setup employed to observe the SN. The GMOS-S instrument is composed of three detectors each covering a different portion of the wavelength range. To obtain a continuous spectrum, almost free from the gaps between the detectors, two spectra of the SN shifted in wavelength were obtained.⁵ A sensitivity function for each detector was employed to calibrate each portion of the spectra independently, these portions were later combined into a single spectrum, thus filling the gaps between the detectors and removing bad pixels.

⁵ For the blue portion of optical spectral range, the B600 grating was employed. The B600 grating combined spectra are free from gaps between detectors. For the red portion was employed the R400 grating with the GG455 second order blocking filter. The red portion of the GMOS combined spectra have a small gap of about 100 Å that affects the O I $\lambda 7774$ line (from +55 to +232 days), or the [Ca II] line in the nebular spectrum at +412 days.

We include in our analysis the classification spectra reported to the TNS by Grzegorzec (2022) and by the ePESSTO+ collaboration. The ePESSTO+ classification spectrum is publicly available and was observed using the EFOSC2 instrument (Buzzoni et al. 1984; Snodgrass et al. 2008) mounted on the New-Technology Telescope (NTT) at La Silla observatory. The ePESSTO+ classification was independently reduced by our team using the PESSTO pipeline (Smartt et al. 2015). The optical spectra are presented in Fig. 3, and a summary of the optical spectroscopic observations of SN 2022jli is presented in Table 3.

2.2.2. Near-infrared

Seven epochs of NIR spectroscopy of SN 2022jli were obtained⁶ using the Flamingos-2 instrument (Eikenberry et al. 2004, 2012) mounted on the Gemini-South telescope. The observations were performed following an ABBA pattern, we observed the *JH* and *HK* configurations that cover from about 8750 to 17000 Å and from 13300 to 24700 Å, respectively. We obtained a *JH* and *HK* pair as close in time as possible to obtain full NIR coverage.

One NIR spectrum of SN 2022jli was obtained using the fourth generation of the Triple-Spec spectrograph (Schlawin et al. 2014) mounted on the NIR Nasmyth platform of the SOAR telescope. Triple-Spec is a cross-dispersed, long-slit spectrograph with a resolution of about 3500, covering the full NIR wavelength range in one observation. The observations were performed following an ABBA pattern. The Triple-Spec spectra were reduced using its custom reduction pipeline, included in the SPEXTOOL IDL package (Cushing et al. 2004). We always observed an A0V telluric star before or after observing the SN and at a similar air mass. After the extraction of the individual spectra, we used the XTELLCORR task (Vacca et al. 2003) included in the SPEXTOOL IDL package (Cushing et al. 2004) to perform the telluric correction and flux calibration of the SN spectra.

3. Analysis

3.1. Host galaxy

NGC 157 is an isolated SAB(rs)bc galaxy, with no close companions of comparable brightness detected in POSS images (Ryder et al. 1998). The galaxy redshift is $z = 0.005500 \pm 0.000002$ (Springob et al. 2005). The SN 2022jli is located in the north-west spiral arm of NGC 157. In this paper we adopt a distance of 23.5 ± 1.6 Mpc, corresponding to the distance derived from the host-galaxy recession velocity by NED considering a correction for Virgo, Great Attractor, and Shapley Supercluster infall (Mould et al. 2000), assuming $H_0 = 70.0$ km s⁻¹ Mpc⁻¹.

3.2. Light curves

3.2.1. Epoch of maximum brightness

We used the unfiltered photometry obtained from the Kleinkaroo Observatory in South Africa and reported by Monard to the TNS to estimate the time of maximum light. In Fig. 5 we show the reported photometry fitted using a second order polynomial to estimate the SN 2022jli maximum brightness. From the polynomial fit we obtained that the epoch of maximum brightness (t_{\max}) was on MJD= 59709.6 \pm 1.2 days at an unfiltered brightness of 14.29 \pm 0.02 mag, where the uncertainties are estimated using the

⁶ 11 individual spectra.

Table 1. Near-infrared photometry of SN 2022jli

Date UT	MJD (days)	Phase (days)	<i>J</i>	<i>H</i>	<i>K_s</i>	Instrument/ Telescope
18-06-2022	59748.3	+38.5	13.71(0.03)	13.12(0.03)	12.94(0.04)	Flamingos-2/Gemini-S
04-07-2022	59764.3	+54.4	13.83(0.01)	13.34(0.01)	13.11(0.02)	Flamingos-2/Gemini-S
05-07-2022	59765.4	+55.5	...	13.38(0.01)	...	Flamingos-2/Gemini-S
27-09-2022	59849.2	+138.8	15.15(0.01)	14.55(0.01)	14.31(0.02)	Flamingos-2/Gemini-S
28-09-2022	59850.1	+139.7	15.17(0.01)	14.54(0.05)	14.35(0.03)	Flamingos-2/Gemini-S
12-10-2022	59864.2	+153.8	15.33(0.01)	14.69(0.01)	14.49(0.02)	Flamingos-2/Gemini-S
19-10-2022	59871.1	+160.6	15.33(0.01)	14.72(0.02)	14.48(0.02)	Flamingos-2/Gemini-S
07-11-2022	59890.1	+179.5	15.65(0.01)	14.97(0.01)	14.74(0.03)	Flamingos-2/Gemini-S
08-11-2022	59891.1	+180.5	15.66(0.02)	Flamingos-2/Gemini-S
09-11-2022	59892.2	+181.6	...	15.00(0.03)	14.78(0.06)	Flamingos-2/Gemini-S
11-11-2022	59894.1	+183.5	15.72(0.01)	15.01(0.03)	14.72(0.01)	Flamingos-2/Gemini-S
17-11-2022	59900.1	+189.5	15.69(0.01)	Flamingos-2/Gemini-S
18-11-2022	59901.1	+223.3	...	14.99(0.01)	...	Flamingos-2/Gemini-S
21-12-2022	59934.1	+223.3	15.90(0.01)	Flamingos-2/Gemini-S
22-12-2022	59935.1	+224.3	...	15.14(0.01)	...	Flamingos-2/Gemini-S
05-01-2023	59949.0	+238.1	16.05(0.01)	15.20(0.01)	14.57(0.02)	Flamingos-2/Gemini-S
03-06-2023	60098.3	+386.6	...	17.36(0.06)	15.52(0.03)	Flamingos-2/Gemini-S
05-06-2023	60100.3	+388.6	19.54(0.06)	17.34(0.05)	15.49(0.04)	Flamingos-2/Gemini-S
26-06-2023	60121.4	+409.6	19.75(0.08)	17.61(0.04)	15.71(0.04)	Flamingos-2/Gemini-S
14-07-2023	60139.3	+427.4	20.04(0.06)	17.81(0.05)	...	Flamingos-2/Gemini-S
15-07-2023	60140.4	+428.4	...	17.76(0.08)	...	Flamingos-2/Gemini-S
30-07-2023	60155.4	+443.4	20.03(0.11)	17.90(0.06)	15.99(0.06)	Flamingos-2/Gemini-S
04-12-2023	60282.0	+569.3	...	19.00(0.18)	16.65(0.09)	Flamingos-2/Gemini-S
04-01-2024	60313.1	+600.2	...	19.29(0.05)	17.15(0.04)	Flamingos-2/Gemini-S

Notes. Numbers in parentheses correspond to 1σ statistical uncertainties. The phase is measured relative to the time of unfiltered maximum brightness.

Table 2. NEOWISE photometry of SN 2022jli

Date UT	MJD (days)	Phase (days)	W1	W2
27-06-2022	59757.5	+47.6	12.87(0.06)	12.53(0.07)
05-12-2022	59919.3	+208.6	14.20(0.08)	12.85(0.07)
26-06-2023	60121.7	+409.8	13.78(0.07)	12.56(0.07)
05-12-2023	60283.5	+570.8	14.16(0.08)	12.83(0.07)

Notes. Numbers in parentheses correspond to 1σ statistical uncertainties. The phase is measured relative to the time of maximum brightness.

Table 3. Summary of optical-wavelength spectroscopic observations of SN 2022jli.

Date UT	MJD	Phase (days)	Instrument/ Telescope	Wavelength Range (Å)	Dispersion (Å/pixel)	Resolution (<i>FWHM</i>) (Å)
22-05-2022	59721.4	+11.7	LDSS-3/Clay	3800 – 10 300	2.0	8.0
24-05-2022	59723.4	+13.7	EFOC2/NTT	3660 – 9240	5.5	23.0
03-07-2022	59763.3	+53.4	Goodman/SOAR	3300 – 7115	2.0	5.5
04-07-2022	59764.3	+54.4	GMOS-S/Gemini-S	4700 – 9750	1.5	6.7
05-07-2022	59765.3	+55.4	GMOS-S/Gemini-S	3550 – 7080	1.0	4.7
11-08-2022	59802.3	+92.2	Goodman/SOAR	3600 – 8950	2.0	5.5
07-10-2022	59859.3	+148.9	LDSS-3/Clay	3800 – 10 300	2.0	8.0
07-11-2022	59890.1	+179.5	GMOS-S/Gemini-S	3560 – 7080	1.0	4.4
07-11-2022	59890.1	+179.5	GMOS-S/Gemini-S	4700 – 9750	1.5	6.8
26-12-2022	59939.1	+228.2	GMOS-S/Gemini-S	3550 – 7080	1.0	4.7
30-12-2022	59943.1	+232.2	GMOS-S/Gemini-S	4700 – 9750	1.0	6.8
17-06-2023	60112.4	+400.6	Goodman/SOAR	3600 – 7020	2.0	9.4
29-06-2022	60124.4	+412.5	GMOS-S/Gemini-S	4600 – 9460	1.5	6.8
05-07-2023	60130.4	+418.5	LDSS-3/Clay	3800 – 10 300	2.0	8.0

Notes. The phase is measured relative to the time of maximum brightness.

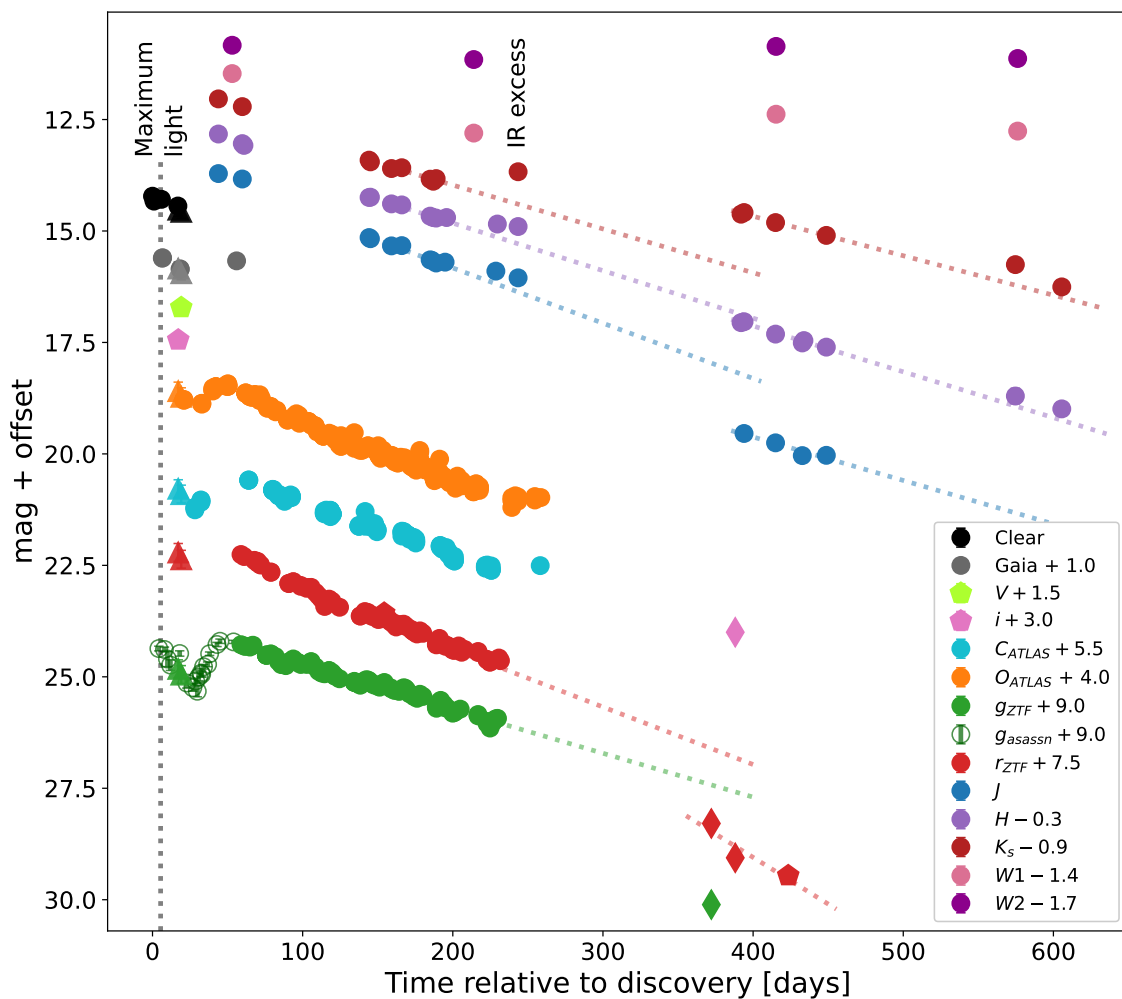


Fig. 2. Optical and NIR light curves of SN 2022jli. Circles correspond to survey photometry or NIR photometry repeatedly obtained using the same instrument or photometric system. Pentagons correspond to photometry computed from LDSS-3 and EFOSC2 spectroscopic acquisition images, diamonds are from late time Goodman photometry and triangles represent synthetic photometry computed from color-matched spectra. The g -band photometry from ASAS-SN is shown using dark-green open circles to avoid confusion with other g -band photometry. The legend on the right specify the colour code and the offsets employed to plot the different bands. Dotted lines are used to compare (extrapolate) the brightness decline from an early epoch to late times in a few relevant bands.

covariance matrix of the polynomial fit. Conservatively, we assume an error on t_{\max} equal to the time lapse between the discovery and the estimated epoch of maximum light, and an error on the brightness equal to the uncertainty on the closest photometric epoch, this is $t_{\max} = 59709.6 \pm 5.4$ days and 14.29 ± 0.05 mag. Our estimate of the epoch of maximum brightness is consistent with the phase reported based on the spectroscopic classification of Grzegorzec (2022).

3.2.2. Secondary maximum and decline rates

SN 2022jli shows double-peaked light curves, and we estimate the epoch of the second maximum by fitting a low order polynomial to the photometry in the g , c and o bands. This procedure yields that the time second maximum took place on MJD equal to 59763.3 ± 8.8 days, 59752.4 ± 2.5 days and 59747.9 ± 1.4 days for the c , o and g -bands, respectively. The time between the first and the second maximum is between +43 to +53 days, the minimum brightness in the g -band reached on 59724.4 ± 1.9 days, coincident with the minimum in the c -band at about +20 days after the first maximum.

After the second maximum a linear polynomial helps to describe the decline of the light curves. We measure the average decline rate of the optical light curves in the time range between the MJD equal to 59790 and 59850, corresponding to a phase between +80 and +239 days relative to the first maximum. The uncertainties are estimated using the Monte Carlo methodology described in Cartier et al. (2022) and used in Hueichapan et al. (2022). The light curve decline rates are summarized in Table 5. The optical bands with bluer effective wavelengths, in this case the g and c bands, decline more slowly than the bands with redder effective wavelengths, the r and o bands, at a significance of 8σ or higher. This is reflected in bluer optical colours at later times (see Section 3.2.5 below), meaning that the ejecta is continuously heated.

From about +200 days the NIR light curves show a re-brightening (see Fig. 2). The NIR photometric coverage allow us to measure the light curve decline rate in two regions, in the MJD range between 59790 and 59900 (+80 to +189 days; before the NIR re-brightening), and in the MJD range between 60090 and 60160 (+378 and +448 days) at late times. The J -band decline is similar to the o -band decline rate before the NIR

Table 4. Summary of NIR spectroscopic observations of SN 2022jli.

Date UT	MJD	Phase (days)	Instrument/ Telescope	Wavelength Range (Å)	Dispersion (Å/pixel)	Resolution (<i>FWHM</i>) (Å)
18-06-2022	59748.3	+38.5	Flamingos-2/Gemini-S	8670 – 17 000	6.5	18
18-06-2022	59748.4	+38.6	Flamingos-2/Gemini-S	13,300 – 24 700	7.6	22
11-08-2022	59802.2	+92.1	Triple-Spec/SOAR	9400 – 24 650	2.2	4.5
27-09-2022	59849.2	+138.8	Flamingos-2/Gemini-S	13,300 – 24 700	7.6	24
27-09-2022	59849.3	+138.9	Flamingos-2/Gemini-S	8780 – 17 000	6.8	18
19-10-2022	59871.0	+160.5	Flamingos-2/Gemini-S	8700 – 17 000	6.4	18
17-11-2022	59900.0	+189.4	Flamingos-2/Gemini-S	8740 – 17 000	6.5	18
18-11-2022	59901.1	+190.4	Flamingos-2/Gemini-S	13,300 – 24 700	7.6	22
21-12-2022	59934.1	+223.3	Flamingos-2/Gemini-S	8750 – 17 000	6.0	18
22-12-2022	59935.1	+224.3	Flamingos-2/Gemini-S	13,300 – 24 700	7.6	22
08-07-2023	60133.4	+421.5	Flamingos-2/Gemini-S	13,300 – 23 800	7.6	24
15-07-2023	60140.4	+428.4	Flamingos-2/Gemini-S	8700 – 17 000	6.5	21

Notes. The phase is measured relative to the time of unfiltered maximum brightness.

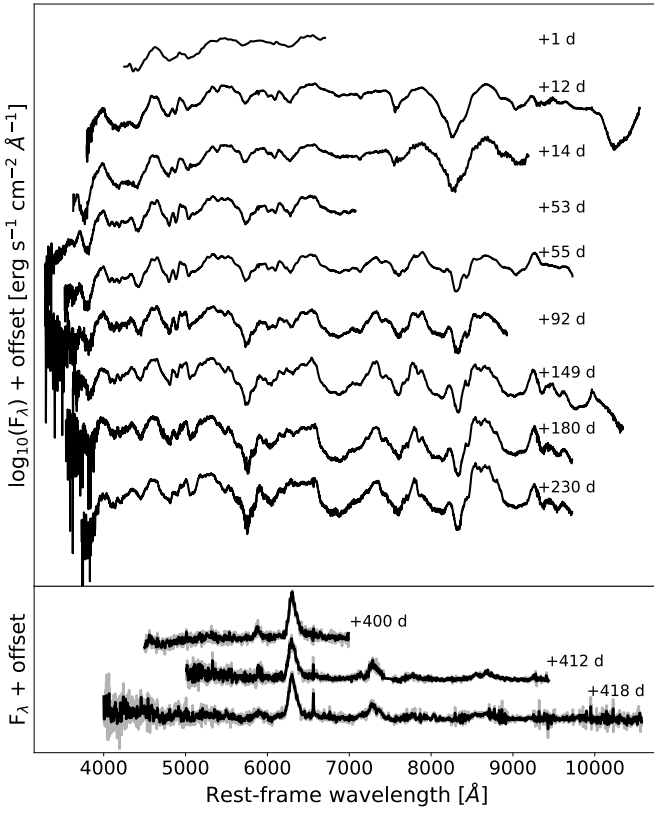


Fig. 3. Optical spectral sequence of SN 2022jli, the phase relative to the time of maximum light is indicated on the right. The spectra during the first +250 days are shown in the top panel in logarithmic scale, the nebular phase spectra are presented in the bottom panel. The smoothed nebular spectra using the Savitzky–Golay filter are shown in black, the original spectra are shown in grey.

re-brightening, and the decline rate trend is the opposite than in the optical bands, with the bluer band, the *J* band, declining faster than the redder *H* and *K_s* bands. The decline rate in the *K_s* band is similar to the *g* band over this range.

At late times (>+350 days) the decline rates in the NIR light curves in all bands are about 1 mag/100 days and are consistent with each other within the uncertainties, while the decline in the *r*-band is about twice the decline measured in the NIR. At later

times the decline rate in the *J* band has become flatter at the 1σ level compared with the decline rate measured at earlier times. Although the NIR emission at late times is dominated by dust thermal emission as we will show in Section 3.4 below, it is worth to note that the decline NIR rates are consistent with the ^{56}Co radioactive decay, while the optical decline rate is much faster.

The linear extrapolation from +80 to +189 days to later times shows that the SN is significantly brighter than the extrapolation in *K_s* (~ 1.2 mag brighter) at later times, similarly the SN brightness in the *H* band is slightly fainter than the linear extrapolation (~ 0.15 mag fainter), and the *J* band brightness is significantly fainter than the linear extrapolation (~ 1.2 mag fainter).

3.2.3. Host-galaxy reddening

The Milky Way reddening in the direction of SN 2022jli is $E(B-V)_{\text{gal}} = 0.0383$ (Schlafly & Finkbeiner 2011). The spectra of SN 2022jli are significantly reddened, showing a clear Na I D narrow absorption feature from the host-galaxy (see Fig. 6), implying that the S suffers significant host-galaxy extinction. The pseudo equivalent width (hereafter *EW*) of Na I was measured in our highest signal-to-noise ratio spectra obtained at a phase before the host-galaxy Na I narrow line spectral region becomes too close to the edge of the underlying broad Na I spectral feature to be properly normalized. The spectra used to measure the Na I *EW* correspond to the LDSS-3, Goodman and GMOS-S spectra obtained at +11.7 days, +53.4 days, and +54.4 days, respectively (see Fig. 6). An average value of $EW = 1.54 \pm 0.12 \text{ \AA}$ was measured for the host Na I D1+D2 feature. Adopting the Poznanski et al. (2012) relation between the *EW* of the host Na I and color excess, implies a host-galaxy color excess of $E(B-V)_{\text{host}} = 0.9 \pm 0.3$ mag. Phillips et al. (2013) note that although a relation between the Na I *EW* and the extinction A_V value exists, the uncertainty in A_V from the Na I *EW* can be significant of the order of 0.3 dex, this is larger than the 0.08 dex quoted by Poznanski et al. (2012). Assuming the uncertainty of Phillips et al. (2013) we obtain $E(B-V)_{\text{host}} = 0.9 \pm 0.7$ mag. Since the Poznanski et al. (2012) relations are calibrated using the original Schlegel et al. (1998) extinction maps, we need to multiply the values derived from Poznanski et al. (2012) relations by 0.86 to place them in the re-calibration of Schlafly & Finkbeiner (2011), then the host galaxy reddening is $E(B-V)_{\text{host}} = 0.8 \pm 0.6$ mag from the Na I D1+D2 absorption feature.

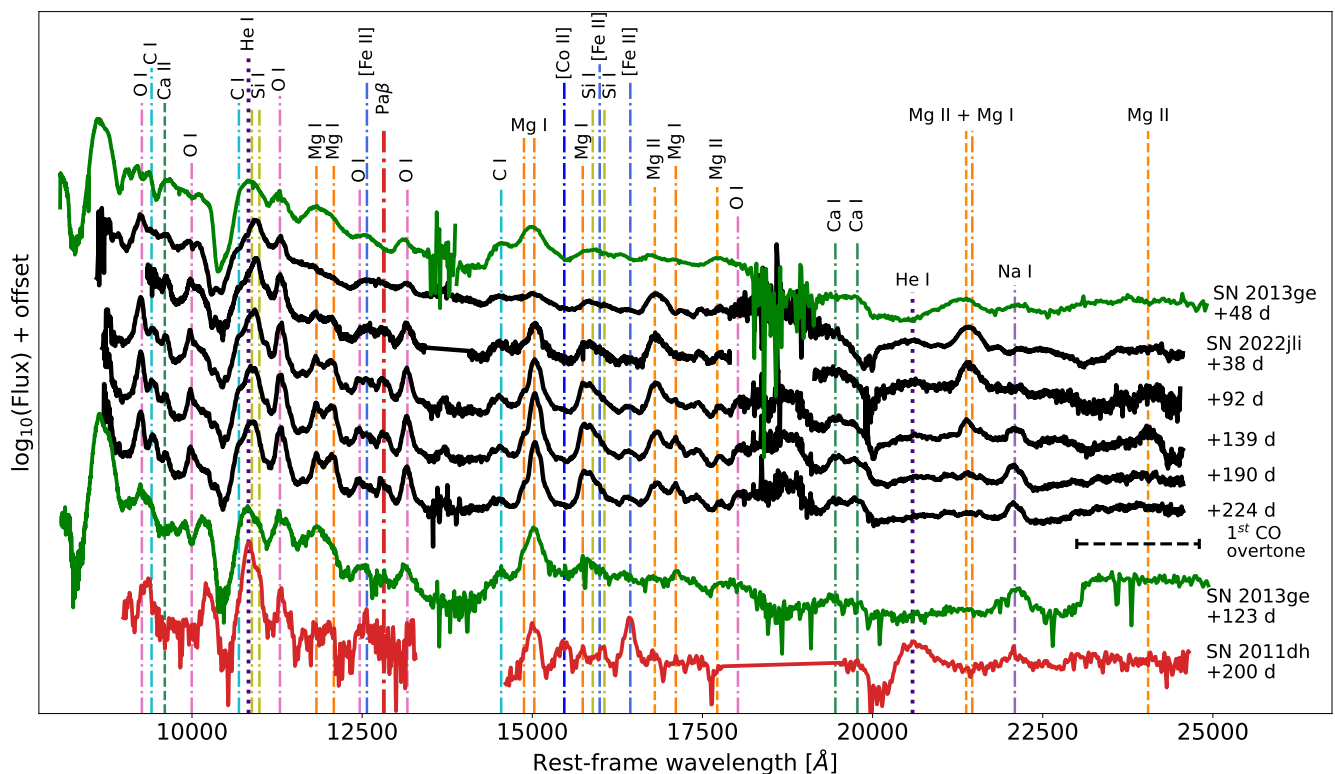


Fig. 4. NIR spectral sequence of SN 2022jli (in black) compared with SN 2013ge (in green; Drout et al. 2016) and SN 2011dh (in red; Ergon et al. 2015). The position of several lines are indicated with vertical lines and the phase relative to the maximum is indicated on the right. Five selected epochs are presented in this figure.

Table 5. Summary of the linear decline rates of SN 2022jli.

Band	Decl. rate (mag/100 days)	Decl. rate (+450 days $>t >+350$ days) (mag/100 days)
Pseudo-Bol	1.12(0.10)	...
<i>g</i>	0.984(0.004)	...
<i>c</i>	1.084(0.012)	...
<i>r</i>	1.290(0.004)	2.09(0.25)
<i>o</i>	1.231(0.012)	...
<i>J</i>	1.239(0.022)	0.98(0.21)
<i>H</i>	1.067(0.066)	1.03(0.11)
<i>K_s</i>	0.984(0.065)	0.89(0.11)

Drout et al. (2011) reported a small scatter of ± 0.06 mag in the $V - R$ colours of SE SNe (Iib/Ib/Ic) around +10 days relative to the V -band maximum. This property was later confirmed by the radiative transfer models of Dessart et al. (2015) and investigated in detail by Stritzinger et al. (2018b) using multi-band photometry of SE SNe (Stritzinger et al. 2018a) from the Carnegie Supernova Project I (CSP-I; Hamuy et al. 2006). Using the CSP-I photometry, Stritzinger et al. (2018b) created unreddened colour templates for SE SNe, for the different sub-types (i.e., Iib, Ib, Ic). According to Stritzinger et al. (2018b) these templates can provide a host reddening estimate with photometry obtained between +0 to +20 days relative to V -band maximum.

We use the LDSS-3 and NTT (ePESSTO+) optical spectra of SN 2022jli obtained at +11.7 and +13.7 days, respectively, to compute synthetic colours. These spectra combined with the CSP-I broad-band transmission curves and zero points from Krisciunas et al. (2017), provide the colour information needed to estimate the SN reddening by means of computing synthetic

photometry. As in Stritzinger et al. (2018b) and throughout this paper, the Fitzpatrick (1999) reddening law is adopted, and in this work $R_V = 3.1$ is assumed. We also assume an uncertainty of 0.075 mag for the synthetic magnitudes, which translates to an uncertainty of 0.10 mag in colour. The total reddening along the line-of-sight ($E(B - V)_{\text{tot}}$), that is the host galaxy and the Milky Way reddening, was inferred as the difference between the synthetic colours and the colour templates.

The reported colour excess value for each colour corresponds to the weighted average of the reddening values obtained for the two spectra. The quoted uncertainties were computed by adding in quadrature the uncertainties in the intrinsic colour-curve templates and in the synthetic colours. Table 6 lists our total and host-galaxy ($E(B - V)_{\text{host}}$) colour excess estimations for SN 2022jli, inferred from nine colour combinations. We used the Fitzpatrick (1999) reddening law with $R_V = 3.1$ to transform from a given colour excess to $E(B - V)$ colour excess.

The host-galaxy reddening estimates derived from the Stritzinger et al. (2018b) colour templates yield values of $E(B -$

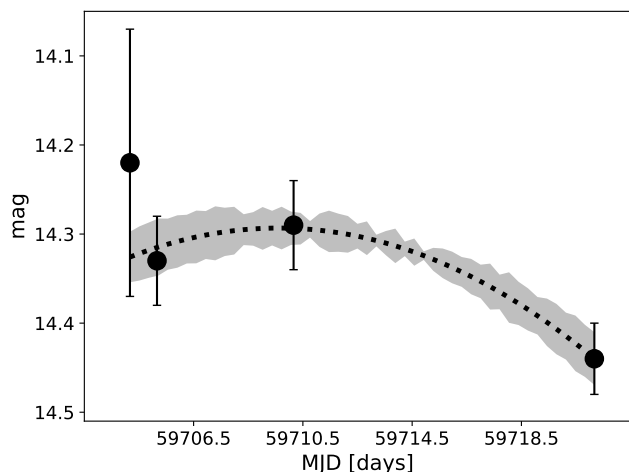


Fig. 5. Unfiltered photometry reported by Monard to the TNS obtained at the Kleinkaroo Observatory in South Africa (black points). The black dotted line corresponds to a second order polynomial fitted to the photometry. The polynomial fit was performed weighting by the photometric uncertainties and the shaded area corresponds to the 1σ uncertainty computed from the covariance matrix of the polynomial fit. From this fit we obtained that the epoch of maximum brightness was on $\text{MJD} = 59709.6 \pm 1.2$ days at an unfiltered brightness of 14.29 ± 0.02 mag, however we assume more conservative uncertainties for these parameters (see text).

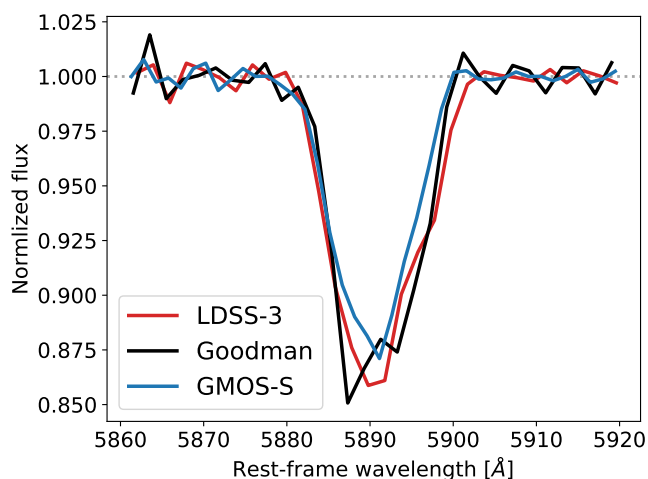


Fig. 6. Normalized host-galaxy Na I D line for SN 2022jli at +11.7 days (LDSS-3/Clay), +53.4 days (Goodman/SOAR) and +54.4 (Gemini-S/GMOS-S). The average equivalent width of the Na I D line for the three epochs is $EW = 1.54 \pm 0.12$ Å.

V_{host} between 0.14–0.62 mag, with the $E(B-g)$ colour being the most discrepant value of $E(B-V)_{\text{host}} = 0.62 \pm 0.20$ mag. Not considering the latter value, which seems to be an outlier, we obtain a weighted mean of $E(B-V)_{\text{host}} = 0.23 \pm 0.06$ mag, where the uncertainty is equal to standard deviation of the $E(B-V)_{\text{host}}$ values. Throughout the paper we assume $E(B-V)_{\text{host}} = 0.23 \pm 0.06$ mag for SN 2022jli, which when tacking on the MW reddening colour excess corresponds to a total value of $E(B-V)_{\text{tot}} = 0.27 \pm 0.06$ mag.

3.2.4. Periodicity in the light curves

After an inspection of the light curves of SN 2022jli it was clear that in addition to the main re-brightening that occurs at 25-

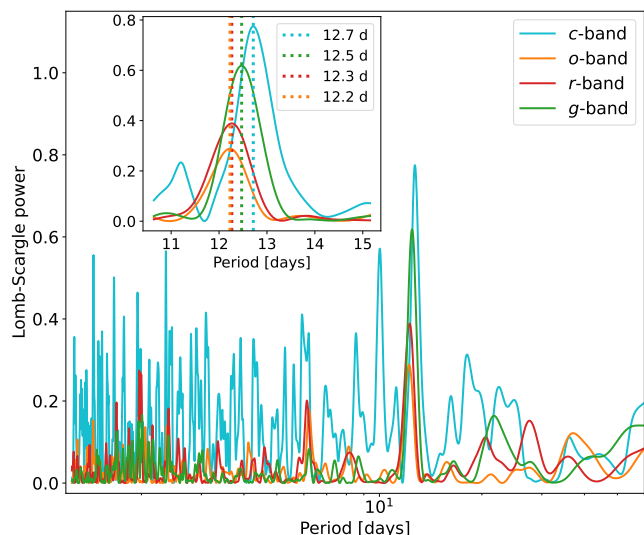


Fig. 7. Lomb-Scargle periodogram of the detrended and normalized g (green), r (red), c (cyan) and o (orange) light curves of SN 2022jli. In the inset we present in detail the region around the peak frequencies.

60 days after maximum light, we can distinguish several softer bumps or undulations, which are clearly detected in the ATLAS and ZTF light curves. We fitted a fifth order polynomial to detrend the ZTF and ATLAS light curves to study the structure of these undulations. For the analysis of the ATLAS light curves we consider observations with uncertainties smaller than 0.15 mag, and weighted averages were computed for the observations obtained within the same night (i.e., observed within 8 hrs difference), this procedure significantly reduces the noise of the ATLAS light curves.

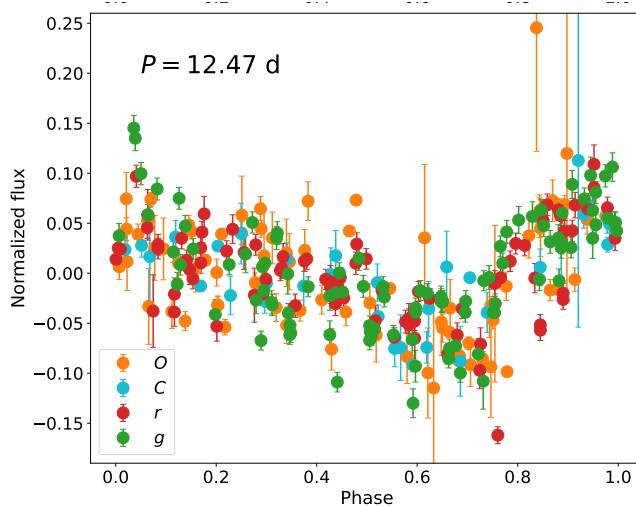
The detrended residuals reveal periodic or quasi-periodic undulations, with the g -band showing larger amplitudes than the r -band. We found that the root mean square of the detrended g -band flux is $1.0 \times 10^{-16} \text{ erg s}^{-1} \text{ cm}^{-2} \text{ Å}^{-1}$ compared with $0.5 \times 10^{-16} \text{ erg s}^{-1} \text{ cm}^{-2} \text{ Å}^{-1}$ in the r -band, thus confirming that the amplitude is larger in the bluer bands. We analyzed the normalized light curve residuals using a Lomb-Scargle periodogram (see Fig. 7) to discover that the periodic signal is stronger in g than in the r -band, with a period of 12.47 days and 12.27 days in the g and r bands, respectively. A similar analysis reveals a period of 12.71 days and 12.23 days in the c and o bands of ATLAS, respectively. Despite the small differences in the period found for the different bands, with bluer (g and c) bands having slightly longer periods than the redder bands (r and o), folding the ATLAS and ZTF light curves to a common period of 12.47 days they show a very good agreement in the periodic variability (see Fig. 8), consistent with Moore et al. (2023) and Chen et al. (2024) results. We adopt this period hereafter in our analysis.

3.2.5. Colour evolution

In Fig. 9 we present the $g-r$ colours of SN 2022jli compared with the colours of the CSP-I SE SN sample Stritzinger et al. (2018a,b), and the double-peaked SE SNe 2005bf (Folatelli et al. 2006), PTF11mnb (Taddia et al. 2018a), SN 2019cad (Gutiérrez et al. 2021) and 2019stc (Gomez et al. 2021). As could be expected, the synthetic colours of SN 2022jli at +12 and +14 days corrected for reddening (see Section 3.2.3) are located at the lo-

Table 6. Summary of reddening determinations for SN 2022jli.

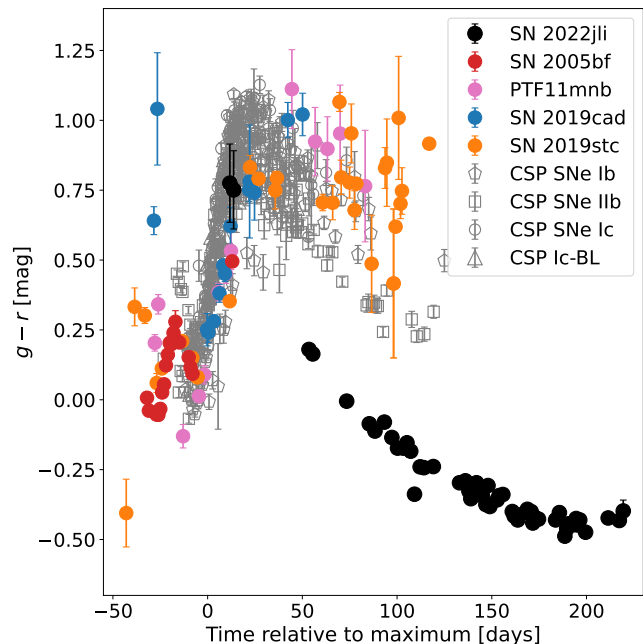
Method	$E(B - V)_{\text{tot}}$	$E(B - V)_{\text{host}}$	Reference
$E(B - g)$	0.66(0.20)	0.62(0.20)	Stritzinger et al. (2018b)
$E(B - V)$	0.32(0.07)	0.28(0.07)	Stritzinger et al. (2018b)
$E(B - r)$	0.31(0.05)	0.27(0.05)	Stritzinger et al. (2018b)
$E(B - i)$	0.30(0.03)	0.26(0.03)	Stritzinger et al. (2018b)
$E(g - V)$	0.17(0.12)	0.14(0.12)	Stritzinger et al. (2018b)
$E(g - r)$	0.18(0.06)	0.14(0.06)	Stritzinger et al. (2018b)
$E(g - i)$	0.22(0.04)	0.18(0.04)	Stritzinger et al. (2018b)
$E(V - r)$	0.18(0.13)	0.15(0.13)	Stritzinger et al. (2018b)
$E(V - i)$	0.27(0.06)	0.23(0.06)	Stritzinger et al. (2018b)
Na I EW	...	0.8(0.6)	Poznanski et al. (2012); Phillips et al. (2013)


Fig. 8. Folded ATLAS and ZTF light curves to a common period of 12.47 days.

cus of the SE SNe intrinsic color-curve evolution from maximum to +20 days.

As can be readily observed in Fig. 9, after the onset of the SN re-brightening (at 20 – 35 days), the SN displays very blue colours compared to the bulk of SE SNe, of ~ 0.65 mag bluer than the bulk of SE SNe at about +50 days. The SN continues evolving to bluer $g - r$ colours until about +190 days after maximum, when a colour minimum is reached. Although all normal SE SNe tend to evolve from red to blue colour after reaching a peak in the $g - r$ colour at about 25-30 days, the extreme colours of SN 2022jli are remarkable. The blue colour is presumably related with the extra power injection which produces the secondary maximum, increasing the ejecta temperature as we discuss in Section 3.2.7 below. If the SN 2022jli is not corrected by Galactic and host-galaxy reddening, the $g - r$ colour of the SN would be ~ 0.25 mag bluer than the bulk of the SE SNe. It is worth noting that SN 2022jli has bluer colours and higher ejecta temperature than the double-peaked SN 2019stc which follows a colour evolution comparable to the bulk of SE SNe. This suggests that the physical mechanism(s) producing the secondary maximum is probably different in these two SNe.

We note that the strong Na I D absorption line is readily noticeable throughout the SN evolution, suggesting that the dust and gas is not destroyed by the SN radiation, or by the potential ejecta-CSM interaction. Unfortunately, at late phases the Na I feature is located at the edge of an underlying broad spectral feature which prevents the most reliable measurement of its EW .


Fig. 9. $g - r$ colours of SE SNe corrected by reddening using the Fitzpatrick (1999) reddening law. SN 2022jli is plotted in black, while in grey are the CSP-I SE SNe (Stritzinger et al. 2018b) with different symbols used for each SE SN sub-types as indicated in the legend. For comparison are also presented the double-peaked SE SN 2005bf (Ib-pec; Folatelli et al. 2006), PTF11mnb (Ic-pec; Taddia et al. 2018a), SN 2019cad (Ic-pec; Gutiérrez et al. 2021) and SN 2019stc (Ic-pec; Gomez et al. 2021).

In Fig. 10 we investigate the colour behaviour during the light curve undulations in detail. We present the total flux emission in the $(g + r)$ bands corrected by reddening, compared with the $g - r$ colours in two well-sampled regions of the ZTF light curves. We find that in addition to becoming blue with time, there is large scatter in the $g - r$ colour showing periodic or quasi-periodic evolution. The peak to trough variation in the $g - r$ colours is of the order of 0.07 to 0.10 mag, which is $5 - 7\sigma$ larger than the 0.015 mag variation expected from the median of colour photometric uncertainty alone. In Fig. 10, we mark the maxima of the $(g + r)$ flux (blue dot-dashed line) and the peaks of the SN colours (red dashed lines), finding that at the epochs of flux maxima the SN tend to be bluer, while at the epochs of $g - r$ colour peaks (redder colours) the SN is (generally) declining in $(g + r)$ flux and close to a flux minima following a periodic or quasi-periodic cycle.

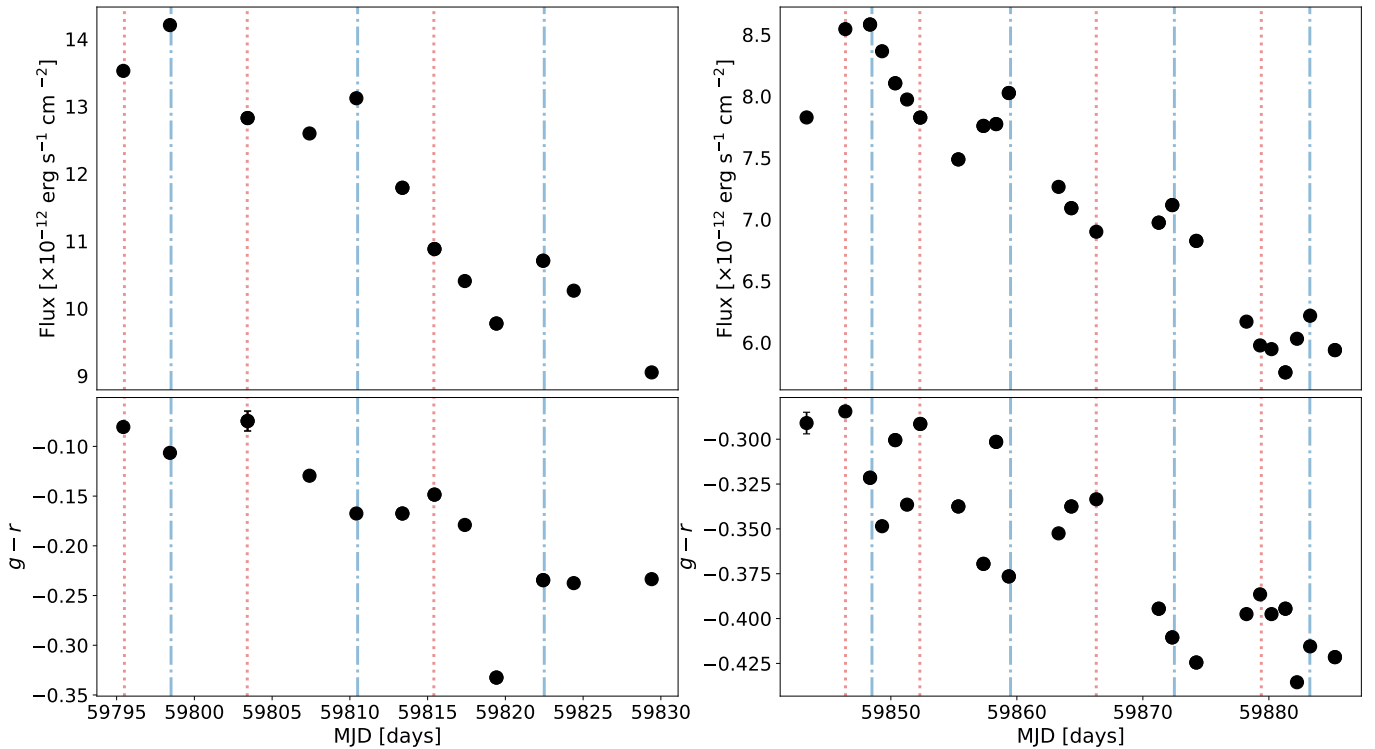


Fig. 10. Top panels: total ($g + r$) flux corrected by reddening ($E(B - V) = 0.27$) following the Fitzpatrick (1999) reddening law for two regions with well-sampled light curves. Bottom panels: $g - r$ colours (corrected by reddening) for the same two regions with well-sampled light curves. The vertical blue dot-dashed lines mark the observed flux maxima, and the vertical red dashed lines mark the color maxima (redder colours). The flux and the colours show periodic undulations.

3.2.6. Light curve comparison

In Fig. 11 the r -band absolute magnitude light curve of SN 2022jli is compared with the well observed SN 2011dh (Ib; Ergon et al. 2014, 2015), SN 2013ge (Ic; Drout et al. 2016) and the SE SNe from the CSP-I (Stritzinger et al. 2018a,b). The absolute magnitude at the first maximum of SN 2022jli is ≈ -17.9 mag⁷ compared with the maxima absolute magnitude of ≈ -17.2 mag of SNe 2011dh and 2013ge. As can be observed, SN 2022jli seems to be a bright SE SN, within the range of normal luminosity SE SNe. After the second maximum, the decline of the SN 2022jli light curve is nearly parallel to the comparison objects, but SN 2022jli is ~ 2.3 mag brighter than the comparison SNe 2011dh and 2013ge. At later times, SN 2022jli suffered a sudden luminosity drop between about 250 and 375 days (see also Chen et al. 2024), and by 400 days the SN spectrum (see Section 3.3.5 below) and brightness in the r band are similar to SN 2013ge.

3.2.7. Bolometric light curve

In Fig. 12 we present the pseudo-bolometric light curve of SN 2022jli. At early times during the first and secondary maximum, the scarcity of multi-band photometric observations poses a problem for the construction of a pseudo-bolometric light curve of SN 2022jli. We circumvent this problem by constructing spectral templates which are scaled in flux, using contemporary photometry to achieve an accurate flux calibration of the

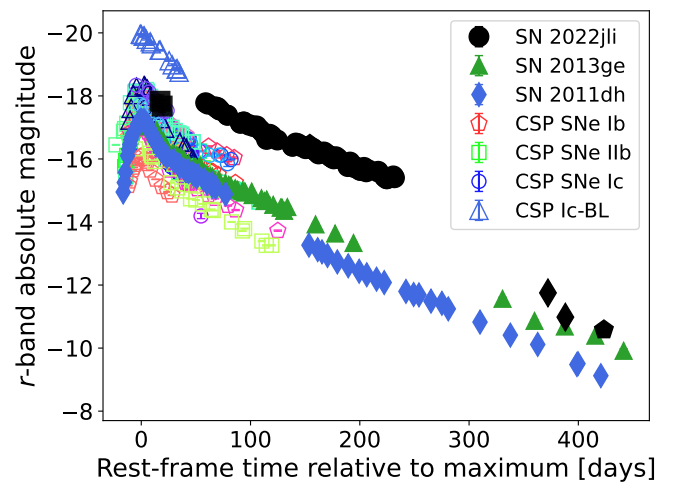


Fig. 11. Comparison between the r -band absolute magnitude of SN 2022jli (black symbols) and well observed SE SNe from CSP-I (open symbols; Stritzinger et al. 2018b), SN 2011dh (blue diamonds; Ergon et al. 2015, 2014) and SN 2013ge (green triangles; Drout et al. 2016). SNe IIb, Ib, Ic and Ic-BL from the CSP-I are shown with open squares, pentagons, circles and triangles, respectively.

templates. The photometry used to scale the spectra was obtained as close in time as possible to the observing epoch of the spectra, usually in the same or within a couple of nights. In a few cases the photometry used to scale the spectra comes from the acquisition images of the spectra. At the minimum of the c -band and the maximum of the o -band we scaled template spectra with a time difference of 9 days and 12 days relative to

⁷ Estimated from the Gaia photometry of SN 2022jli close to maximum ($G = 14.60$ mag), after correcting by reddening in the line-of-sight.

the time of the photometry, respectively. We consider it important to have an estimate of the SN luminosity at these phases. In Section 3.3 we show that the spectra vary slowly during at this time (see spectra between +14 and +55 days in Fig. 3), and it is accounted in the bolometric error the uncertainty introduced by the use spectra and photometry with a relevant time difference (see Appendix). As shown in Section 3.3 and in the Appendix, the spectrum of SN 2022jli after maximum light is similar to the spectra of SN 2013ge at a similar phase. We exploited this similarity to estimate the bolometric luminosity of SN 2022jli close to maximum light, by employing the template spectrum of SN 2013ge at maximum constructed carefully and scaled in flux using the Gaia photometry of SN 2022jli at +1.4 days (see the Appendix for more details). The maximum light spectral template of SN 2013ge was carefully color-matched to the photometry of SN 2013ge and corrected by reddening along the line-of-sight to SN 2013ge. Then, the reddening free spectral template of SN 2013ge was reddened by the reddening in the line-of-sight to SN 2022jli and scaled to the photometry of SN 2022jli close to maximum light.

We estimate the NIR contribution at the first maximum and during the decline from it using spectrophotometric templates of SN 2013ge. These optical-NIR templates were constructed by colour matching the optical spectra to the photometry, and the NIR spectra were scaled to the optical spectra in their overlapping regions (from 8000 – 9500 Å approximately). We estimate that the NIR contribution is of the order of 10 – 15% of the total optical and NIR emission during this phase. From +38 days the NIR contribution was estimated directly from the NIR photometry of SN 2022jli, and is of the order of 7 – 9% until ~ 230 days. At about +380 days the NIR corresponds to 59% of the SN emission.

The bolometric light curve of SN 2022jli is double-peaked, with both maxima reaching a similar bolometric luminosity of about $3 \times 10^{42} \text{ erg s}^{-1}$.⁸ The estimated decline rate from the first maximum is $3.67 \pm 0.94 \text{ mag}/100 \text{ days}$, and the decline rate after the second maximum is $1.18 \pm 0.10 \text{ mag}/100 \text{ days}$. At later times the SN showed a significant drop in luminosity, and the pseudo-bolometric luminosity becomes dominated by the NIR emission (corresponding to 60%).

A black-body model was fitted to the optical spectra of SN 2022jli after scaling them and matching their colours to the photometry. The estimated black-body temperature (T_{bb}) and radius (R_{bb}) are shown in Fig. 12. During the decline from the first maximum the ejecta temperature is $\sim 5000 \text{ K}$ and $R_{bb} \simeq 2.7 \times 10^{15} \text{ cm}$ ($\simeq 39000 R_{\odot}$). After the second maximum the ejecta temperature increases and the R_{bb} shows a decrease with time reaching a minimum of $R_{bb} \simeq 6 \times 10^{14} \text{ cm}$ ($\simeq 8600 R_{\odot}$) at about +150 days and staying constant thereafter. The ejecta temperature reaches a maximum temperature of $\simeq 9000 \text{ K}$ at about +150 days, and the ejecta temperature decreases thereafter.

3.2.8. ^{56}Ni and ejecta mass

In order to estimate the mass of the ejecta (M_{ej}) and of the radioactive ^{56}Ni (M_{Ni}) produced by the SN, we used the Arnett (1982) analytical solution for type I SNe, assuming that the first maximum is powered by the radioactive decay of ^{56}Ni and employing the methodology described in Cartier et al. (2022). We fitted the bolometric light curve of SN 2022jli from the first max-

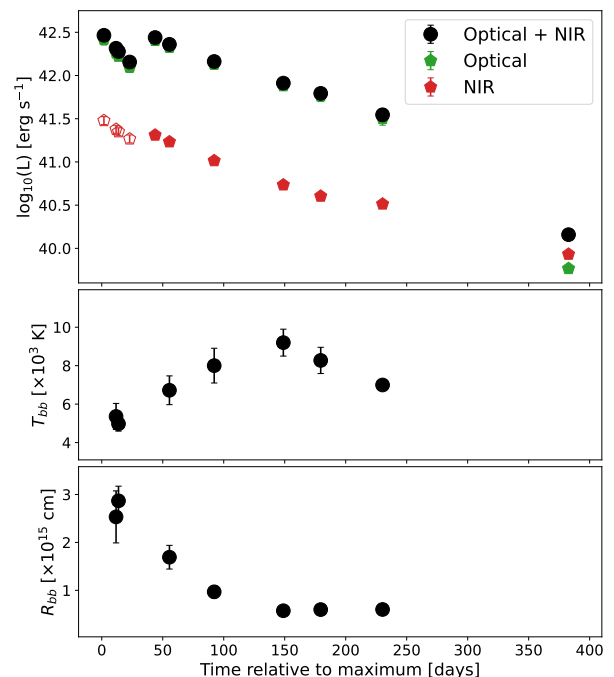


Fig. 12. Top: pseudo-bolometric light curve of SN 2022jli (black circles) computed integrating the SN spectra in the optical region between 3800 – 9000 Å (green pentagons) and taking in account the NIR contribution (red pentagons). The NIR emission during the decline from the first maximum was estimated from optical+NIR templates of SN 2013ge as described in the text, and these estimates are shown using open pentagons. The pseudo-bolometric luminosity at +383 days was estimated directly from the *griJHK_s* photometry. Middle: T_{bb} computed from a black-body fit to the spectra of SN 2022jli. Bottom: R_{bb} from a black-body fit to the spectra of SN 2022jli.

imum to the minimum at about +20 days, assuming an ejecta velocity at maximum light of $v_{ej} = 8500 \text{ km s}^{-1}$ (see Section 3.3.4), an optical opacity of $\kappa = 0.07 \text{ cm}^2 \text{ gr}^{-1}$ and a rise time to maximum light of $\tau_{rise} = 14 \text{ days}$. This rise time provides the best fit to the bolometric light curve measured using the reduced χ^2 . The rise time to maximum calculated for SN 2022jli is also consistent with the typical rise times measured in normal SNe Ic. For example, Taddia et al. (2015) reports average rise times in the *r*-band of $22.9 \pm 0.8 \text{ days}$, $21.3 \pm 0.4 \text{ days}$, $11.5 \pm 0.5 \text{ days}$ and $14.7 \pm 0.2 \text{ days}$ for SNe IIb, Ib, Ic and Ic-BL from SDSS-II, respectively. Although Arnett’s analytical solution has limitations (see e.g., Khatami & Kasen 2019), like the assumption of a constant optical opacity, the Arnett’s model remains a widely used, simple and powerful analytical model to obtain reasonable estimates for M_{ej} and M_{Ni} . Following Taddia et al. (2018b), it is assumed $\kappa = 0.07 \text{ cm}^2 \text{ gr}^{-1}$, since it provides consistent results for the M_{ej} and M_{Ni} parameters when the Arnett’s analytical model is compared with the hydro-dynamical models of Bersten et al. (2011, 2012), both fitted to the bolometric light curves of the CSP-I sample (see Taddia et al. 2018b, for a discussion).

Figure 13 presents the analytical fit to the first bolometric peak of SN 2022jli. Given that the rise to maximum of SN 2022jli is not constrained, we explored a range of τ_{rise} from +10 to +23 days, which comprises the range of typical τ_{rise} found in SNe Ibc (see Taddia et al. 2015). It was found that 14 days provides the best analytical fit for SN 2022jli, with good fits having τ_{rise} in the range of 11 to 17 days. In this range of τ_{rise} the analytic solution provides an ejecta mass (M_{ej}) and a radioactive ^{56}Ni mass (M_{Ni}) that do not significantly vary. The values obtained

⁸ The SN reached a luminosity of $2.9 \pm 0.4 \times 10^{42} \text{ erg s}^{-1}$ in the first maximum and a luminosity of about $2.8 \pm 0.3 \times 10^{42} \text{ erg s}^{-1}$ in the second maximum.

for SN 2022jli are $M_{\text{ej}} = 1.51 \pm 0.40 M_{\odot}$, $M_{\text{Ni}} = 0.12 \pm 0.01 M_{\odot}$, where the quoted errors reflect the uncertainty in the assumed τ_{rise} and v_{ej} . The good quality of the fit to the first maximum of the bolometric light curve, the fact that M_{ej} and M_{Ni} are typical of a standard SN Ic and that SN 2022jli shows spectral features of a SN Ic, supports the idea that the first maximum of SN 2022jli is a standard SN Ic mainly powered by the decay of ^{56}Ni .

As noted previously, at later times the SN shows a drop in luminosity, which marks a decrease in the power injection from the energy source producing the second maximum. This might be a consequence of the well known drop in the ejecta opacity to γ -rays at late times, due to the expansion of the SN ejecta. This is illustrated in Fig. 13 with the rapid decline of the UVOIR light curve of SN 2011dh (Ergon et al. 2015) after maximum light. SN 2011dh is chosen for comparison because is a normal SE SN (type Iib) with a high-quality and well-sampled UVOIR light curve, constructed from high-quality and well-sampled optical and infrared observations from the U -band to the mid-IR *Spitzer* S_2 -band collected from +4 days until about +400 days. SN 2011dh has an estimated $M_{\text{Ni}} = 0.075 M_{\odot}$, and its decline rate after maximum is significantly faster than the decline rate expected of full trapping from the ^{56}Co decay, the daughter product of ^{56}Ni . As in the case of SN 2011dh, a significant fraction of the power from the ^{56}Co radioactive decay probably escape after maximum in SN 2022jli.⁹

3.3. Spectra

3.3.1. Spectral comparison

In Fig. 14, SN 2022jli is compared with other SE SNe at about +12 days, during the decline from maximum brightness and before its re-brightening. SE SNe are classified as Type Iib, Type Ib and Type Ic depending on the presence of clear and unambiguously detectable amounts of hydrogen and helium in the SN ejecta. At this phase, the spectral features of SN 2022jli correspond to a SN Ic very similar to SN 2013ge during its decline from maximum light. The spectra of SN 2022jli do not show strong helium or Balmer absorption lines such as in SN 2007Y (Ib) and in SN 2011dh (Iib). A comparison with the bumpy SLSN-I SN 2019stc shows that this SLSNe exhibit a bluer continuum and broader spectral lines yielding more blended spectral features compared to their lower luminosity cousins like SN 2022jli.

A manifestation that the envelope stripping is probably not complete is that some SNe Ib exhibit small amounts of hydrogen material (see e.g., Holmbo et al. 2023; Dong et al. 2023) and some SNe Ic show evidence of helium in their ejecta (see e.g., Drout et al. 2016; Shahbandeh et al. 2022; Holmbo et al. 2023). This is also the case of SN 2013ge that although it is classified as a SN Ic, it shows weak He I features in the optical and in the NIR (see Drout et al. 2016) and has an estimated ejecta mass of 2-3 M_{\odot} , not far from the estimated ejecta mass of SN 2022jli. Similarly, SN 2022jli also shows weak He I features as discussed below (see also Moore et al. 2023). Additionally, a double peaked, weak and variable $H\alpha$ feature is robustly detected after the second maximum. This spectral feature shows a periodic shift in its peak following the light curve undulations and it seems to be a manifestation of the accretion of hydrogen rich material from a companion star in a binary system (Chen et al. 2024). The Ic classification of SN 2022jli is reinforced by

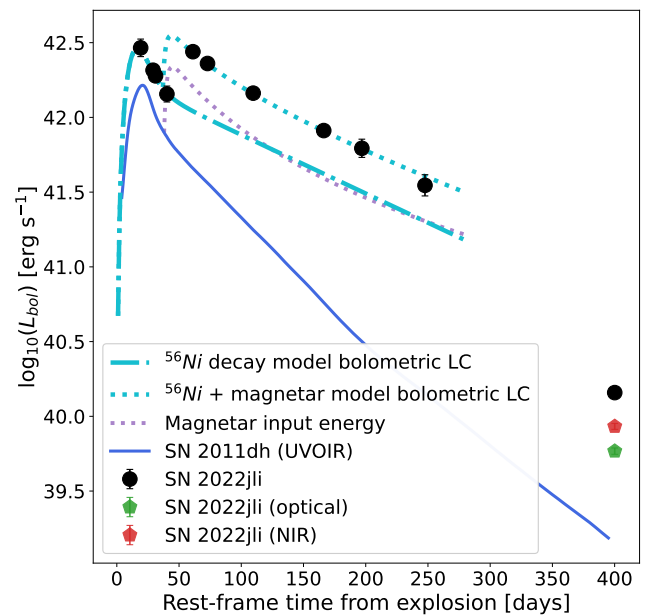


Fig. 13. Fit of the radioactive decay of ^{56}Ni to the first maximum of the bolometric light curve of SN 2022jli, using the Arnett (1982) analytic approximation. The parameters of the best-fit model are $\tau_{\text{rise}} = 14$ days, $M_{\text{ej}} = 1.51 M_{\odot}$, $M_{\text{Ni}} = 0.12 M_{\odot}$, $v_{\text{ej}} = 8500 \text{ km s}^{-1}$ and $\kappa = 0.07 \text{ cm}^2 \text{ gr}^{-1}$. This model illustrates that the first maximum of SN 2022jli is consistent with the typical rise time, ^{56}Ni and ejecta mass of a normal SN Ic. The secondary maximum is modelled as the sum of the radioactive decay of ^{56}Ni and the spin-down energy from a magnetar (dotted cyan line; see Cartier et al. 2022, for details about the magnetar model). To model the secondary maximum the magnetar birth is delayed 37 days relative to the assumed time of the SN explosion and the magnetar parameters are $B = 8.5 \times 10^{14} \text{ G}$ and $P = 48.5 \text{ ms}$. The purple dotted line shows the magnetar contribution to the bolometric light curve. The optical and NIR luminosity at +383 days are shown using green and red pentagons, respectively. The pseudo-bolometric (UVOIR) light curve of the well-observed SE SN 2011dh (Iib) is shown for comparison ($M_{\text{Ni}} = 0.075 M_{\odot}$; Ergon et al. 2015).

its nebular spectrum (see Fig. 14), where SN 2022jli displays differences with the nebular spectra of SNe Iib and Ib, which are discussed in detail below.

Close to the time of the second maximum, the spectral features of SN 2022jli do not show a significant evolution (see Fig. 15). At this phase, the spectrum of SN 2022jli still shows a clear pseudo-continuum, and a few (pseudo-)nebular features begin to appear in the red part of the optical spectrum, such as [Ca II] $\lambda\lambda 7291, 7323$ and O I $\lambda 7774$. In turn, the spectral features in the blue part of the optical region ($< 7000 \text{ \AA}$) remain essentially the same, and remain almost unaltered for the next 100 days after maximum light, evolving very slowly.

Between +45 and +65 days normal SNe Ic become pseudo-nebular, the continuum becomes redder and not so strong. Spectral features of [Ca II] $\lambda\lambda 7291, 7323$, and a strong Ca II NIR P-Cygni emission are clearly present, and a weak [O I] $\lambda\lambda 6300, 6364$ feature can be distinguished. In turn, the Ca II NIR triplet in SN 2022jli is shallower than in the comparison SE SNe, and even compared with the same SN during its decline from the first maximum. All of this is a consequence of the extra energy input which makes the pseudo continuum bluer compared with other SE SNe. The [O I] $\lambda\lambda 6300, 6364$ doublet is absent in SN 2022jli at this epoch, and it may weakly contribute to the SN spectrum after +150 days. However, the [O I] doublet seems to

⁹ After 200 days, is expected that practically all γ -ray photons from the electron capture process will escape (see e.g., Milne et al. 1999).

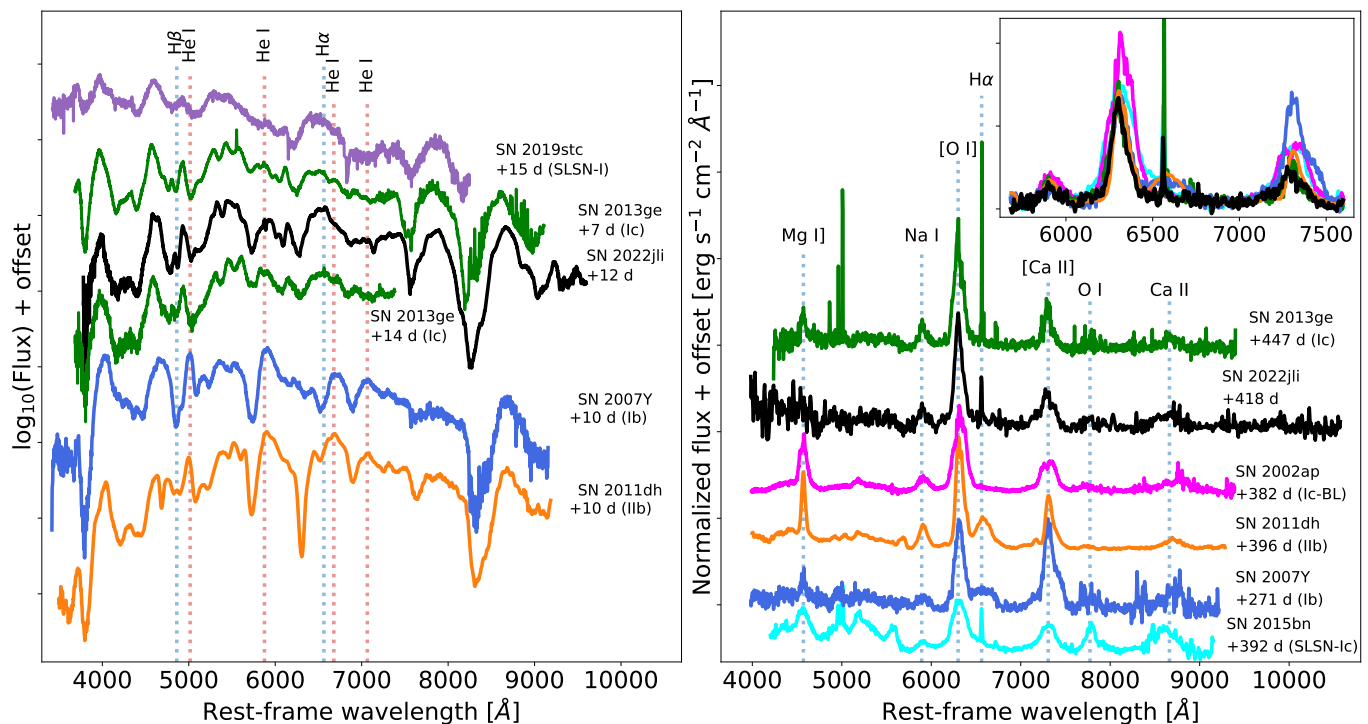


Fig. 14. Comparison of SN 2022jli with other SE SNe in decline from the first maximum and at a late nebular phase. On the left panel, SN 2022jli is compared at about +12 days relative to the first maximum, during the decline from maximum light, with the bumpy SLSNe-I SN 2019stc (Gomez et al. 2021), the Ic SN 2013ge (Drout et al. 2016), the Ib SN 2007Y (Stritzinger et al. 2009, 2023) and the Iib SN 2011dh (Ergon et al. 2014). Similarly, on the right panel, SN 2022jli is compared with the SLSNe-I SN 2015bn (Nicholl et al. 2016a), the Ic-BL SN 2002ap (Shivvers et al. 2019), SN 2013ge and SN 2011dh (Ergon et al. 2015) at nebular phase. We indicate the rest-frame wavelength of the main spectral features. All the spectra have been corrected for reddening assuming $R_V = 3.1$ and values from the literature, in the case of SN 2022jli we assume $E(B-V)_{\text{tot}} = 0.27$ mag.

appear after +200 days in the SN spectrum and it becomes the strongest optical spectral feature by +400 days (see Fig. 14).

In the right-panel of Fig. 15 we compare SN 2022jli with other SE SNe at 150 days. At this phase SN 2022jli is becoming pseudo-nebular, a decrease in the continuum can be appreciated at wavelengths redder than 5500 Å, but still shows a blue continuum compared to normal luminosity SE SNe, its continuum shape is more similar to SLSNe-Ic. The shape of the spectral features, on the other hand, is more similar to SE SNe rather than to SLSNe. At this phase SE SNe are in the nebular phase showing spectra dominated by [O I] $\lambda\lambda 6300, 6364$ and [Ca II] $\lambda\lambda 7291, 7323$ lines as shown in Fig. 15.

In summary the evolution of the optical spectra of SN 2022jli after the re-brightening resembles the evolution of SLSNe-I in the sense that these SNe show a slow evolution and bluer continuum compared to normal luminosity SE SNe. However, SN 2022jli has stronger spectral features typical of a SN Ic, whereas SLSNe-Ic have shallower and broader spectral features (see Fig. 15 and Cartier et al. 2022, for a discussion). The spectral features displayed by SN 2022jli and by all normal SNe Ic show less blending than most SLSNe-Ic, pointing to a less energetic explosion of SN 2022jli than SLSNe-Ic.

Presented in Fig. 4 is the NIR spectral sequence of SN 2022jli starting at +38 days relative to the first maximum and continuing for nearly +200 days. As in the optical, SN 2022jli evolves slowly in the NIR. We identify strong lines of O I, C I, Mg I, Mg II, Na I, weak lines of He I $\lambda 2.058$ and Pa β as discussed below, and potential lines of Si I. Weak lines of [Fe II] seem to appear between 100 and 200 days, these lines are commonly observed in most core-collapse SNe. Initially, at +38 days, we iden-

tify that the strongest spectral features in the H and K_s bands correspond to Mg II. As the Mg II lines fade, the Mg I spectral features become stronger.

3.3.2. Helium

The optical spectra of SN 2022jli do not show unambiguous He I lines, but the potential presence of a small amount of helium is suggested by the strong absorption feature at about 5730 Å, which is usually associated with the Na I D line in SNe Ic, but in this case the absorption feature seems to be strengthened by presence of the He I $\lambda 5875$ line (see Fig. 14). In addition, a weak spectral feature coincident with He I $\lambda 7065$ from about $\sim +50$ days (see Fig. 15) also suggests the presence of small amounts of helium. The existence of helium in the SN ejecta is further supported by a very weak broad spectral feature barely detected at $\sim 2.058 \mu\text{m}$ in the NIR spectra at +36 and +92 days (see also Tinyanont et al. 2024). As discussed in Dessart et al. (2020) and Shahbandeh et al. (2022), the He I $\lambda 2.058$ line is probably the best suited spectral feature for an unambiguous detection of helium in SNe Ic.

3.3.3. Hydrogen

SN 2022jli shows a broad and blended spectral feature at the location of H α (Fig. 16), and a double peaked profile at the location of the Pa β (Fig. 17). From about the time of the second maximum the H α feature begins to show a double peaked profile (see Fig. 16). The peaks of the double horned profiles in the

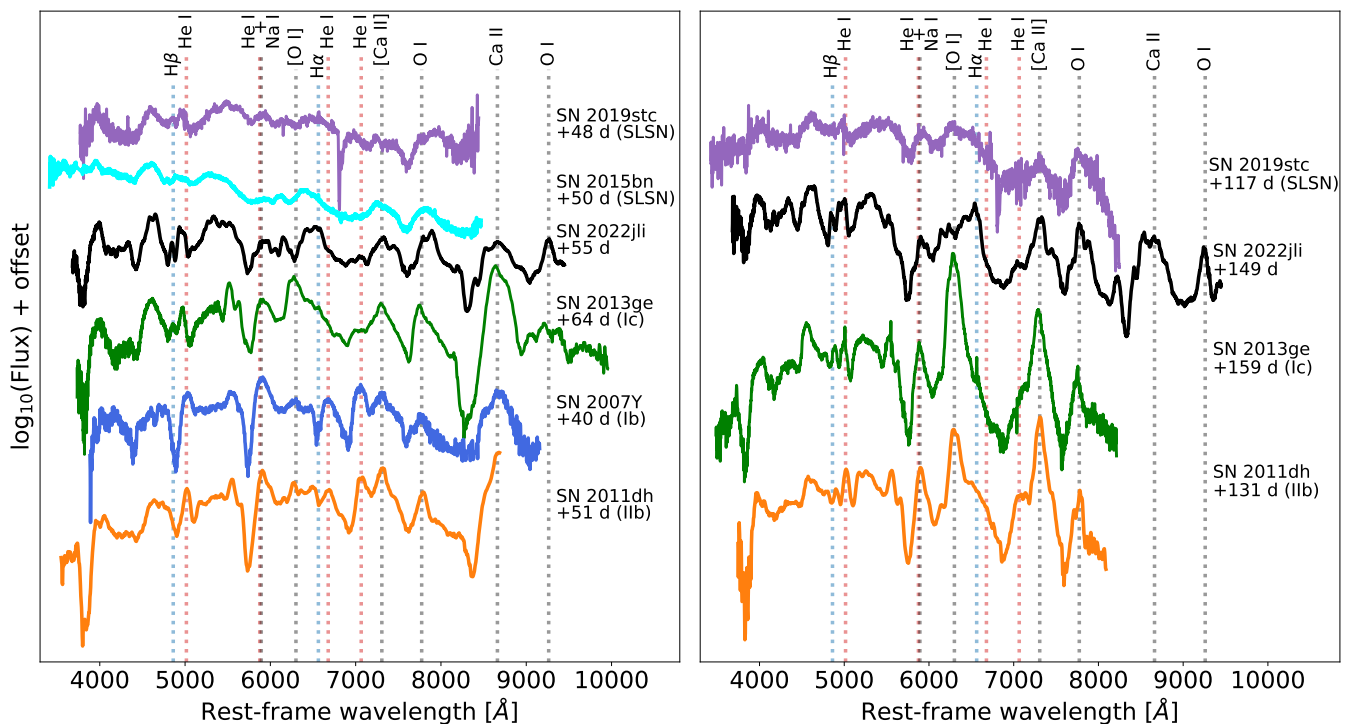


Fig. 15. Comparison of SN 2022jli with other SE SNe during the SN re-brightening. On the left panel, the SN is compared at the time of its second maximum with the SLSNe-I SN 2019stc (Gomez et al. 2021) and SN 2015bn (Nicholl et al. 2016b), the Ic SN 2013ge (Drout et al. 2016), the Ib SN 2007Y (Stritzinger et al. 2009, 2023) and the IIb SN 2011dh (Ergon et al. 2014) at a similar phase relative to the first maximum. Similarly, on the right panel, SN 2022jli is compared with SN 2019stc, SN 2013ge and SN 2011dh (Ergon et al. 2015) at about +149 days relative to the first maximum. We indicate the rest-frame wavelength of the main spectral features. All the spectra have been corrected for reddening assuming $R_V = 3.1$ and values from the literature, in the case of SN 2022jli we assume $E(B - V)_{\text{tot}} = 0.27$ mag.

$H\alpha$ and $Pa\beta$ features are located at about ± 1000 km s $^{-1}$ from the central rest-frame line position (see Figs. 16 and 17).

The evolution of the $H\alpha$ profile is presented in Fig. 16. A pseudo-continuum on each side of the profile has been used to subtract the underlying continuum emission, and the resulting residuals were normalized by the median residual flux over the region. On the left-panel, the spectra at +12 and +14 days are compared with the spectra of SN 2013ge at a similar phase. There is a potential excess emission at $\sim +800$ km s $^{-1}$, however the overall profile is very similar to the profile of SN 2013ge and no clear evolution in the shape of the spectral feature is detected between the two epochs. Therefore the presence of $H\alpha$ emission is ambiguous during the decline from the first maximum.

On the right panel, the $H\alpha$ profile from about the time of the second maximum until +232 days are presented, ordered by phase assuming a period of 12.47 days. The spectra obtained close to the secondary maximum (53–55 days) and at +92.2 days (ϕ in range of 0.28 – 0.44) show a double peaked profile similar to the one first detected at +92.1 days in the $Pa\beta$ line, but there is no apparent shift in the line profiles over this phase. In the spectra at $>+100$ days, the double peaked feature becomes more conspicuous and shows a clear shift in the peak position with phase. The latter is probably due to the larger phase coverage in the spectra after 100 days (ϕ from 0.30 to 0.94).

The $Pa\beta$ profile is not detected in the NIR spectrum at +38.5 days, and only becomes evident in the spectrum at +92.2 days (see Fig. 17), after the time of the secondary maximum. The feature becomes more conspicuous with time as can be observed in Fig. 4. The maxima of the double peaked profile seem to shift as function of the phase of the periodic undulations and consistent with the variation observed in the $H\alpha$ fea-

ture at $>+100$ days (Fig. 17). No other hydrogen lines are clearly detected in the NIR spectra of SN 2022jli. For example, we inspected in detail the region of $Br\gamma$ and the line is not visible despite of the good signal-to-noise ratio of the NIR spectra. Some weak hydrogen lines may be blended with lines of other species. The $H\alpha$ and the $Pa\beta$ lines produce relatively weak spectral features indicative of a small amount of hydrogen, and the double peaked profiles could be a consequence of an accretion disk or of out-flowing material ejected in winds. At +400 days the SN spectrum is fully nebular and spectral feature associated with $H\alpha$ is no longer detected, supporting the conclusion that the amount of hydrogen material mixed in the ejecta is very small, if any.

Narrow $H\alpha$ emission lines are present in the nebular spectra obtained with the GMOS-S and LDSS-3 spectrographs at late times, this narrow emission is not present in the nebular spectrum obtained a few days before with the Goodman spectrograph. In the 2D spectra several narrow emission lines from the host galaxy are observed, therefore this narrow $H\alpha$ emission line is most likely originated in an H II region in the host galaxy close to the SN position. Although it seems unlikely, the potential appearance of late time narrow hydrogen lines such as in SN 2016adj (Stritzinger et al. 2024) cannot be completely discounted.

3.3.4. Expansion velocity

As previously discussed, SN 2022jli shows spectral features of a SN Ic after maximum light and throughout its evolution. Now we pay attention to the ejecta expansion velocity. We estimate the ejecta velocity from the minimum of the Fe II $\lambda 4923.9$, Fe II $\lambda 5001.9$ and Fe II $\lambda 5169.0$ absorption lines. In table 7 we sum-

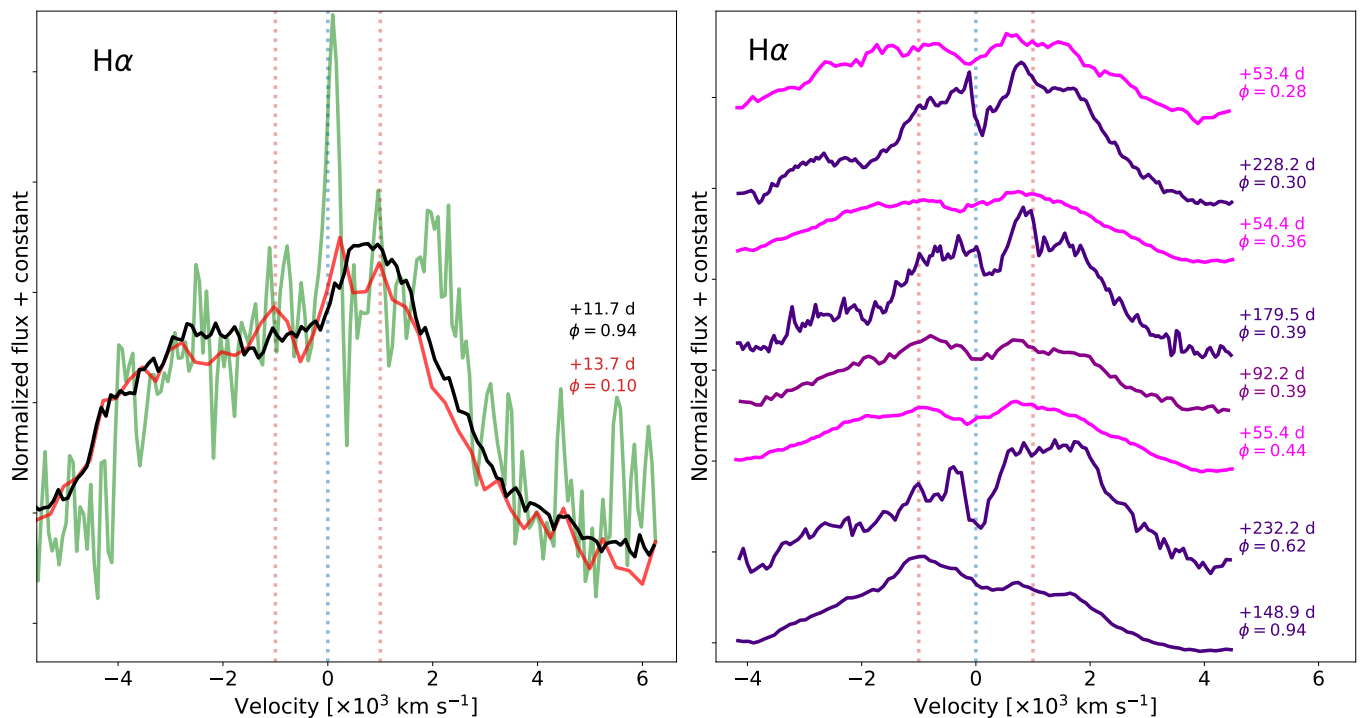


Fig. 16. Velocity profile of the region around the $H\alpha$ spectral feature. A pseudo-continuum on each side of the profile has been used to subtract the underlying continuum emission, and the result was normalized by the median residual flux over the region. On the left panel, the spectral region of SN 2022jli during the decline from the first maximum is compared with SN 2013ge (in green) at a similar spectral phase of $\sim 12 - 14$ days. On the right hand panel, the evolution of the $H\alpha$ velocity profiles of SN 2022jli from +53 days to +232 days are shown, during and after the second maximum, ordered with respect to the phase folded period of 12.472 days (ϕ). The near maximum spectra are shown in magenta, the intermediate phase spectrum at +92.1 days spectrum is shown in dark magenta and the late phase spectra ($>+100$ days) is shown in indigo. The phase with respect to maximum and the periodic phase (ϕ) are indicated on the right of each spectrum. Red dotted vertical lines indicate a velocity of $\pm 1000 \text{ km s}^{-1}$ for comparison.

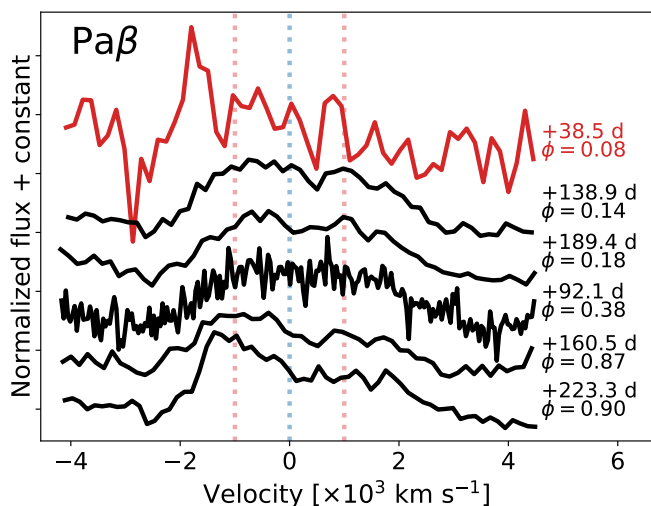


Fig. 17. Velocity profile of the region around the $Pa\beta$ spectral feature in the NIR. As in the case of $H\alpha$, a pseudo-continuum on each side of the profile has been used to subtract the underlying continuum emission, and the result was normalized by the median residual flux over the region. Red dotted vertical lines indicate a velocity of $\pm 1000 \text{ km s}^{-1}$ for comparison.

marise the ejecta velocity estimated from each of these three lines, and provide their weighted average. The uncertainty of the weighted average corresponds to the maximum value between

the error from the weighted mean and the standard deviation from the three independent measurements.

Figure 7 compares the ejecta expansion velocity of SN 2022jli with the normal type Ic SN 2007gr and SN 2013ge. For these three SNe, the ejecta velocity was estimated using the Fe II lines. Taddia et al. (2018b) shows that the Fe II velocity evolution from early times, before maximum light, to late times can be described with a power law. Here we show that from about +10 days the ejecta velocity is well described by a linear decline, assuming that the velocity decline rate for these three SNe was measured in a time window between +10 and +100 days. We found that the velocity decline rates are $13.5 \pm 0.8 \text{ km s}^{-1} \text{ day}^{-1}$ for SN 2022jli, $44.9 \pm 5.8 \text{ km s}^{-1} \text{ day}^{-1}$ for SN 2013ge and $17.0 \pm 0.6 \text{ km s}^{-1} \text{ day}^{-1}$ for SN 2007gr. The expansion velocity of SN 2022jli after maximum is comparable to other SNe Ic, and extrapolating linearly its velocity to maximum light a value of $v_{\text{Fe II}}^{\text{avg}} \approx 8250 \text{ km s}^{-1}$ is obtained, the true value must be slightly higher given the power-law behaviour of the ejecta velocity at early times. The velocity decline rate post-maximum of SN 2022jli follows a linear evolution marginally slower than the comparison SNe. The latter suggest that the physical mechanism producing the secondary maximum and the undulations has a moderate effect on the expansion velocity of the ejecta. Arguably the main effect is to inject energy to the ejecta keeping a pseudo-photosphere for longer time at a higher ejecta velocity compared with normal SNe Ic. The latter effect is evident at about 100 d, when the comparison SNe Ic are almost fully nebular, and the non-nebular Fe II lines are no longer detected. The linear extrapolation of the ejecta velocities of the

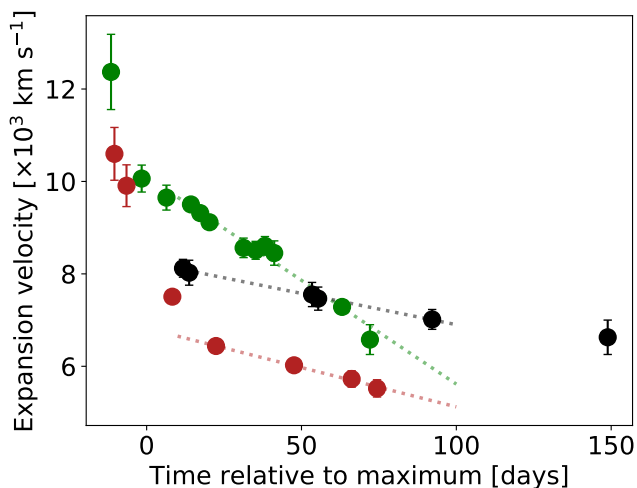


Fig. 18. Expansion velocity estimated from the Fe II lines (see text) for SN 2022jli (black), SN 2013ge (green) and SN 2007gr (red). The dashed lines illustrate the velocity decline rate, measured between +10 and +100 d, for the three SNe.

comparison Ic's at +100 days are slower ($\leq 6000 \text{ km s}^{-1}$) than the ejecta velocity of SN 2022jli at this phase ($\approx 7000 \text{ km s}^{-1}$).

3.3.5. Nebular phase

In Fig. 15 the spectrum of SN 2022jli at +418 days is compared with the spectra of other SE SNe at nebular phase. SN 2022jli appears like a normal SN Ic similar to SN 2013ge. The strongest spectral features of SE SNe at this phase are [O I] $\lambda\lambda 6300, 6364$ and [Ca II] $\lambda\lambda 7291, 7323$.

We investigated the [O I] and [Ca II] profiles of SN 2022jli, using Gaussian profiles to fit the lines. The continuum emission regions were defined selecting the minimum on each side of the spectral features, and a linear polynomial was fitted between these regions to subtract the continuum emission. In SN 2022jli, the [O I] line does not show any contamination from other lines such as H α or [N II] as is frequently observed in some Type IIb and Ib SNe, and the [O I] doublet was modelled using two Gaussian profiles fixing the ratio between the two components to 3:1, assuming an optically thin nebular emission as in Taubenberger et al. (2009). The [Ca II] lines show a weak but clear contamination from the [Fe II] $\lambda 7155$ line on the blue part of the profile, and can also be contaminated by other relatively weak [Fe II] and [Ni II] lines in this region. We assumed that the [Fe II] $\lambda 7155$ emission can be well described by a Gaussian profile, the profile was fitted using blue part of the [Fe II] $\lambda 7155$ line, which does not seem to be affected by the [Ca II] emission. Making use of the Gaussian fit, the flux contribution from the [Fe II] $\lambda 7155$ line was subtracted from the [Ca II] spectral feature.

The [O I] emission line of SN 2022jli does not require an additional component, and it does not show a double peaked profile found in some SE SNe (see e.g., Maeda et al. 2008; Taubenberger et al. 2009; Fang et al. 2022; Prentice et al. 2022). At +400 days the centre of the doublet is blue-shifted by -274 km s^{-1} and has a $\text{FWHM} = 3610 \text{ km s}^{-1}$ (corrected by the instrumental resolution). At +412 days the [O I] doublet is blue-shifted by -294 km s^{-1} and has a $\text{FWHM} = 3700 \text{ km s}^{-1}$ (corrected by the instrumental resolution), and the [Ca II] is red-shifted by $+250 \text{ km s}^{-1}$ and has a $\text{FWHM} = 4800 \text{ km s}^{-1}$ (corrected by the instrumental resolution). It is important to note that the [Ca II] line on the GMOS-S nebular spectrum at

+412 days is affected by a gap between the detectors on the red tail of the line. The ratio between the [O I] and the [Ca II] lines is 2.1 at +412 days. In the same way at +418 days the centre of the doublet is blue-shifted by -336 km s^{-1} and has a $\text{FWHM} = 3776 \text{ km s}^{-1}$ (corrected by the instrumental resolution), and the [Ca II] is red-shifted by $+430 \text{ km s}^{-1}$ and has a $\text{FWHM} = 6100 \text{ km s}^{-1}$ (corrected by the instrumental resolution). The ratio between the [O I] and the [Ca II] lines is 2.2 at +418 days. For comparison, at +447 days the center of the [O I] doublet is blue-shifted by -495 km s^{-1} in SN 2013ge and has a $\text{FWHM} = 4400 \text{ km s}^{-1}$ (corrected by the instrumental resolution), and the [Ca II] doublet is blue-shifted by -979 km s^{-1} and has a $\text{FWHM} = 4780 \text{ km s}^{-1}$. The ratio between the [O I] and the [Ca II] lines is 2.7 in SN 2013ge.

Prentice et al. (2022) studied the [O I]/[Ca II] ratio for a sample of 86 SNe from the literature, finding that this ratio does not evolve significantly between about 200 days and +400 days in normal luminosity CC SNe, and that the different sub-types are found in well-localised range of values. For example, SNe II have [O I]/[Ca II] ratios in the range 0.3 – 1.4 with a median 0.5, SNe IIb are found in the range of 0.5 – 3.3, SNe Ibc in the range of 1.0 – 5.0, while SLSNe-I are found in a wide range of values overlapping with II and IIb SNe. The [O I]/[Ca II] = 2.2 ± 0.1 for SN 2022jli confirms its SE SN nature, and places this object within the Ibc range.

3.4. Carbon monoxide emission and late-time near-infrared excess

The formation of carbon monoxide (CO) is key in the process of molecule and dust formation in the SN ejecta, playing an important role in cooling the SN ejecta (Liljegren et al. 2020) to temperatures at which dust can form and in the process of molecule formation. The CO molecule is readily detectable in late time NIR spectra of SNe from its 1st CO overtone emission in the spectral region between 2.3 and 2.5 μm (e.g., Spyromilio et al. 1988; Elias et al. 1988; Gerardy et al. 2002; Hunter et al. 2009; Drout et al. 2016; Banerjee et al. 2018; Rho et al. 2018, 2021; Tinyanont et al. 2019; Stritzinger et al. 2024). The fundamental CO mode at about 4.6 μm is frequently detected in the small number of CC SNe observed at late-times in the mid-IR (e.g., SN 1987A, SN 2004dj, SN 2004et, SN 2005af and SN 2017eaw; see Catchpole et al. 1988; Meikle et al. 1989; Kotak et al. 2005, 2006, 2009; Szalai et al. 2011; Tinyanont et al. 2019).

In Fig. 19 the 1st CO overtone spectral feature of SN 2022jli is compared with other CC SNe with clear 1st CO overtone emission. The 1st CO overtone feature is detected for first time in SN 2022jli at +190 days, where the CO overtone band-heads can be clearly distinguished (see Fig. 19). Compared with other CC SNe, the 1st CO overtone emission in SN 2022jli is relatively weak, and it is significantly weaker than in the type Ic SN 2013ge, and similar to the 1st CO emission of SN 2016adj. The potential detection of CO emission at earlier times is ambiguous. For example, at +139 days we can distinguish a broad spectral feature at the expected location, but it seems to be dominated by the emission from the Mg II $\lambda 24048$ line and the characteristic CO band-heads are not distinguishable. At around 400 days the 1st CO emission is no longer detected in SN 2022jli, at this phase the K_s -band is dominated by dust thermal emission (see Fig. 20).

The IR photometry of SN 2022jli reveals a flattening in the JHK_sW1W2 emission at around 200 days (see Fig. 2), which is more evident in the redder IR bands. This IR-excess in SN 2022jli is illustrated in the $H - K_s$ colour diagram of Fig. 20,

Table 7. Summary of the Fe II expansion velocity of SN 2022jli.

MJD (days)	Phase (days)	$v_{\text{Fe II}, \lambda 4923.9}$ (km s ⁻¹)	$v_{\text{Fe II}, \lambda 5001.9}$ (km s ⁻¹)	$v_{\text{Fe II}, \lambda 5169.0}$ (km s ⁻¹)	$v_{\text{Fe II}}^{\text{avg}}$ (km s ⁻¹)
59721.4	+11.7	8332(99)	7888(73)	8250(77)	8121(193)
59723.4	+13.7	8296(243)	7642(371)	7886(277)	8025(270)
59763.3	+53.4	7664(47)	7065(98)	7565(92)	7553(262)
59765.3	+55.4	7701(22)	7113(25)	7556(52)	7464(250)
59802.3	+92.2	7291(238)	6766(288)	6995(101)	7015(215)
59859.3	+148.9	7279(155)	6466(148)	6516(75)	6628(372)

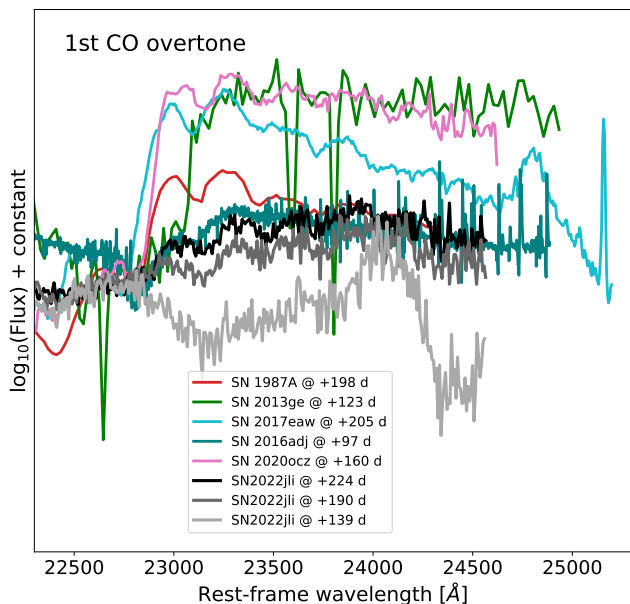


Fig. 19. Comparison of the 1st CO overtone region of SN 2022jli at +139, +190 and +224 days with the with nebular phase CO emission from the type Ic SNe 2013ge (Drout et al. 2016) and SN 2016adj (Stritzinger et al. 2024), and the type II SNe 1987A (Bouchet et al. 1991), 2017eaw (Rho et al. 2018) and 2020ocz (Cartier et al. 2021). The phase and the SN colour are indicated in the inset.

where a jump in the $H - K_s$ colour of ~ 0.35 mag between +180 and +238 days marks the onset of dust emission. The SN continues evolving to extremely red $H - K_s$ colours over the course of the following year, which is a consequence of the dust cooling and of the predominance of the dust thermal emission over the SN ejecta emission.

As shown in the right panel of Fig. 20, despite of the red SN colour, the SN emission in the J and H bands at +238 days is still dominated by the SN ejecta emission. Five months later, at a phase of about +380 days, the ejecta emission has significantly faded and the NIR emission is now dominated by thermal dust emission (see Fig. 20). A NIR spectrum at around +420 days, reveals that the J band still displays broad nebular spectral features from the SN ejecta, however the emission in the H and K_s bands is dominated by dust thermal emission.

Assuming optically thin dust emission, we fitted the H , K_s and $W1$ (when available) photometry using the expression

$$F_\nu = \frac{M_d B_\nu(T_d) \kappa_\nu(a)}{d^2}, \quad (1)$$

where $\kappa_\nu(a)$, the dust mass absorption coefficient, is

$$\kappa_\nu(a) = \left(\frac{3}{4\pi\rho a^3} \right) (\pi a^2 Q_a(a)). \quad (2)$$

Here a is the dust radius, ρ is the dust density and Q_a is the dust absorption efficiency. Here we study two cases, a single-crystal size graphite dust composition where the Q_a was computed by Draine (2016) using the discrete dipole approximation, and a single size silicate dust composition (forsterite) with the Q_a computed using the 1/3-2/3 approximation (Draine & Lee 1984; Laor & Draine 1993). The $W2$ band shows an excess of emission compared with the dust models for both compositions, this band is probably affected by the emission from the fundamental CO band which is coincident with the effective wavelength of the $W2$ band ($4.6 \mu\text{m}$) and is not included in the fits.¹⁰ The evolution of the graphite and silicate dust temperature (T_d), mass (M_d) and luminosity (L_d) for SN 2022jli assuming a dust radius of $a = 0.1 \mu\text{m}$ are presented in Fig. 21. In this figure, a decrease in T_d and L_d parameters can be observed with time. This trend in the evolution is independent of the dust size and composition assumed. The weighted mean for M_d is $2.5 \pm 1.3 \times 10^{-4} M_\odot$ for graphite dust and $10.1 \pm 3.0 \times 10^{-4} M_\odot$ for forsterite silicate dust, both for single size crystals of a radius of $a = 0.1 \mu\text{m}$. In the fitting of the photometry we consider a significant range in the dust radius, finding that for dust particles with a radius $a \leq 0.2 \mu\text{m}$ variations of $<20\%$ in M_d are observed. When larger dust radii are considered $a \geq 0.3 \mu\text{m}$ the M_d is scaled down by a factor of ~ 0.5 compared with the reference radius of $a = 0.1 \mu\text{m}$, for both graphite and silicate dust.

We consider the M_d evolution in more detail. In the case of dust formation in the SN ejecta M_d usually increases with time. An increase of M_d with time is observed in the fits that include $W1$ -band photometry (black symbols in Fig. 21), while a decreasing trend in M_d is observed in the fits performed using only H and K_s photometry. The inclusion of $W1$ photometry practically does not alter our estimates, but reduce significantly the uncertainty, in particular in the fits at +570 days. The observed decrease in M_d in the fits performed to only the H and K_s bands is largely due to the last measurement, with a difference between the earliest and the last (minimum) value of 1.8σ , independent of the dust radius and composition assumed. Future infrared observations of SN 2022jli with the *James Webb Space Telescope* (*JWST*) have the power to constrain the dust composition of the emitting dust, to reveal the presence of more than one dust component, for example dust emission at a cooler temperature (e.g., Kotak et al. 2009; Szalai et al. 2011; Shahbandeh et al. 2023) and to provide a precise evolution of the total dust mass emitting

¹⁰ This IR excess at about $4.6 \mu\text{m}$ due to emission from the fundamental CO band has been previously observed in several SNe (e.g., SN 1987A, SN 2004dj, SN 2004et and SN 2017eaw; see Catchpole et al. 1988; Kotak et al. 2005, 2009; Szalai et al. 2011; Tinyanont et al. 2019).

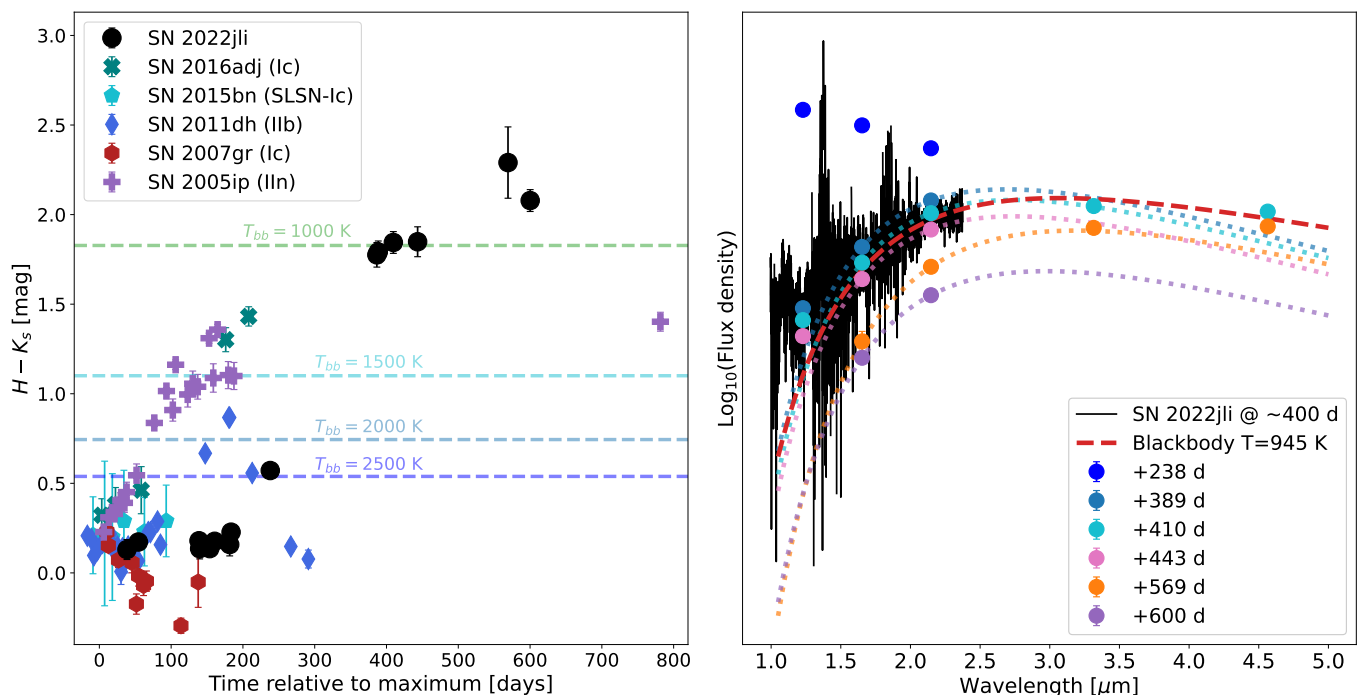


Fig. 20. Left panel: $H - K_s$ colour evolution of SN 2022jli (black circles) compared with the colour evolution of the type Ic SN 2016adj (teal X symbols; Stritzinger et al. 2024), SLSN 2015bn (cyan pentagons; Nicholl et al. 2016b), type IIb SN 2011dh (blue diamonds; Ergon et al. 2014, 2015), the type Ic SN 2007gr (red hexagons; Hunter et al. 2009) and the type IIn SN 2005ip (purple plus sign; Stritzinger et al. 2012). The horizontal dashed lines correspond to the $H - K_s$ colour of a given black-body temperature as indicated in the figure for comparison. Right panel: evolution of the NIR spectral energy distribution (SED) of SN 2022jli from +238 to +600 days. A full NIR spectrum of SN 2022jli at around +422 days is presented, and for comparison a black-body SED having $T = 945$ K is presented for comparison (red dashed line). The dotted lines correspond to dust SED fitting results to the H , K_s and $W1$ photometry of graphite dust with a radius of 0.1 \AA , using the Q_{abs} from Draine (2016).

in the infrared. *JWST* observations are fundamental to fully understand the nature and the composition of the dust emission in SN 2022jli revealed by the infrared observations presented here.

Fitting a linear relation to the $\log_{10}(L_d)$ vs. time shown in Fig. 21, and integrating the luminosity evolution of dust over the time range between 387 and 600 days, we place a lower limit of 8.0×10^{47} erg to the energy radiated by graphite dust and of 2.5×10^{48} erg for the energy radiated by silicate dust. The decline rate luminosity for graphite and silicate dust are $0.5 \text{ mag}/100$ days and $0.3 \text{ mag}/100$ days, respectively.

In Fig. 22, we compare the K_s -band absolute magnitude (M_K) evolution of different local SNe with well observed photometry in the NIR bands. With the exception of SLSNe which are intrinsically brighter and have broad light curves in all bands, bright emission in the K_s band ($M_K < -16$ mag) at late times ($> +200$ days) can be considered a signature of strong dust emission. Normal SE SNe decline faster, while SN 2022jli has a broad M_K light curve with the second maximum powered by an extra energy source. SN 2016adj is a peculiar and bright SE SN showing relatively broad NIR light curve ($M_K \geq -16$ mag at +208 days) and narrow hydrogen emission lines at late times, the latter is a potential signature of ejecta-CSM interaction. SN 2022jli displays a broad light curve somewhat similar to SLSNe-Ic, and shows a decline steeper than the strongly interacting SN 2005ip, which remains bright at an almost constant M_K for several hundred days.

The process of dust formation and the heating mechanism of the dust detected in SN 2022jli is not obvious, the dust may be newly formed in the ejecta or pre-existing dust in the CSM. The first scenario is emission from hot newly condensed dust in the SN ejecta or in a cool dense shell (CDS) produced by the interac-

tion of the ejecta forward shock with a CSM shell. Alternatively pre-existing CSM dust may be radiatively heated by the SN luminosity, by the emission from the first and/or second maxima, producing dust thermal emission, denominated infrared echo.

4. Discussion

A diverse set of mechanisms have been proposed to explain bumps and double-peaked light curves in SNe. Until recently, two main scenarios were usually invoked to explain double-peaked light curves, one is the power injection from a compact object such as a fast spinning neutron star with a strong magnetic field (see e.g., Maeda et al. 2007) or fall-back accretion onto a compact object of stellar mass, like a black-hole or a neutron star. Alternatively, double-peaked light curves and bumps have been frequently considered smoking gun signatures of interaction with a dense circum-stellar medium. In the following we analyse the potential scenarios to explain the strong bump displayed by SN 2022jli and its subsequent undulations.

4.1. Super-Eddington accretion

Recently, Chen et al. (2024) proposed that the second maximum and the subsequent periodic undulations observed in SN 2022jli are the result of the mass accretion from a companion star onto a compact object in a binary system at their periastron encounters. In this paper, the estimated (pseudo) bolometric luminosity of

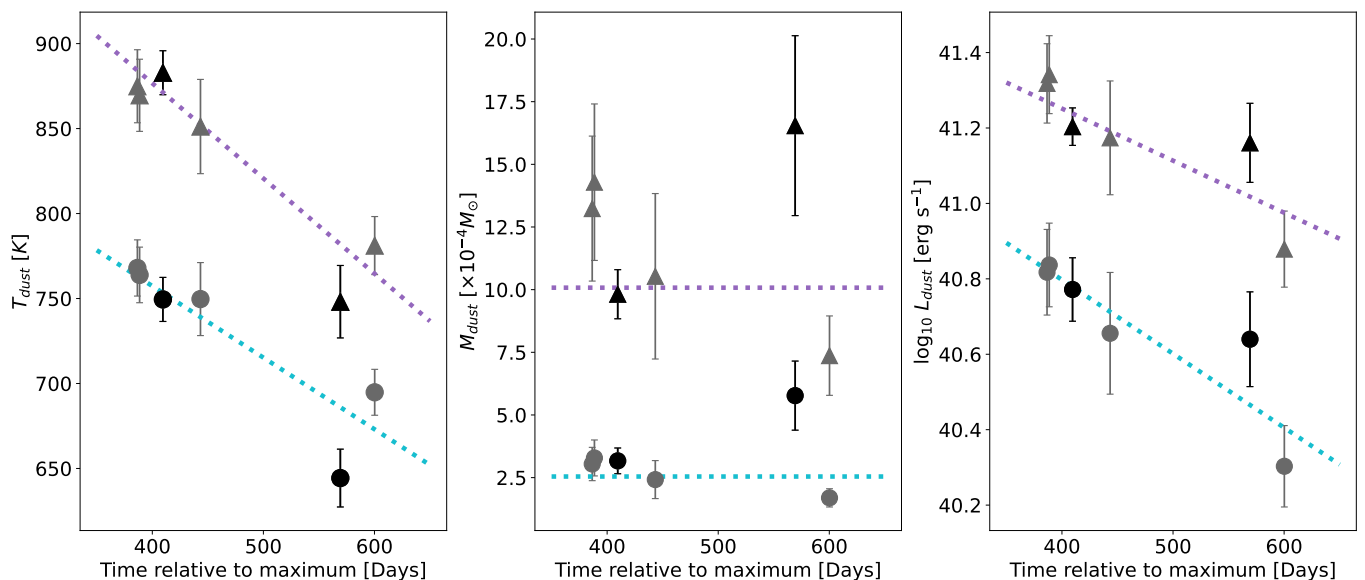


Fig. 21. Evolution of the dust temperature, mass and luminosity as function of time relative to maximum light for silicate (triangles) and graphite (circles) dust, assuming a dust radius of $0.1 \mu\text{m}$. Black symbols correspond to fits performed to H , K_s and $W1$ photometry and grey symbols to fits performed using only H and K_s photometry. Dotted magenta and cyan lines correspond to linear fits to T_d and $\log_{10}(L_d)$ for silicate and graphite dust, respectively. The dotted cyan and magenta horizontal lines indicate the weighted means for M_d of $2.5 \pm 1.3 \times 10^{-4} M_{\odot}$ and $10.1 \pm 3.0 \times 10^{-4} M_{\odot}$ for graphite and silicate dust, respectively.

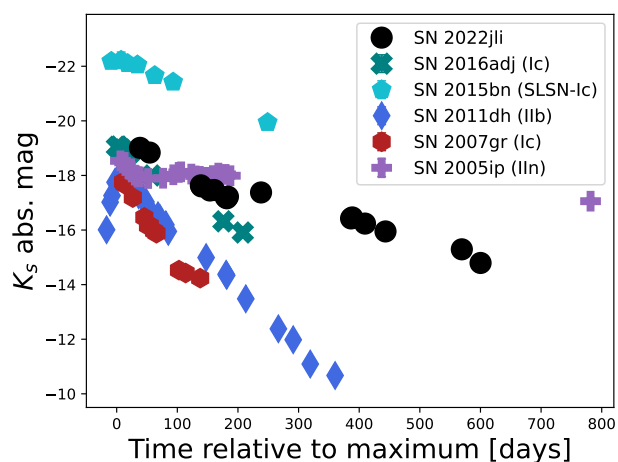


Fig. 22. Comparison of the M_K between SN 2022jli and well observed core-collapse SNe in the NIR bands.

the second maximum is $\sim 1.7 \times 10^{42} \text{ erg s}^{-1}$,¹¹ for a black-hole of $M_{\text{bh}} = 10 M_{\odot}$ or a neutron star of $M_{\text{ns}} = 1.4 M_{\odot}$, respectively.

Super-Eddington accretion into a compact object has been considered as the most likely possibility to explain Ultra-Luminous X-rays sources (ULXs; see Kaaret et al. 2017, for a review), such as NGC 5907 ULX (Israel et al. 2017). These sources can reach X-ray luminosities in excess of a few $10^{39} \text{ erg s}^{-1}$, which is the Eddington luminosity (L_{Edd}) for a $10 M_{\odot}$ black-hole. NGC 5907 ULX is one of the brightest examples of this class, reaching a luminosity of $\sim 2 \times 10^{41} \text{ erg s}^{-1}$, and it might harbor a binary system composed of a neutron star ac-

¹¹ Discounting the energy from the radioactive decay of $0.12 M_{\odot}$ of ^{56}Ni and assuming full trapping of positrons and γ -rays. The full trapping assumption most likely overestimates the power input to the light curve from the $^{56}\text{Ni} \rightarrow ^{56}\text{Co} \rightarrow ^{56}\text{Fe}$ decay chain after maximum light.

creting at $\sim 10^3$ times the L_{Edd} from the companion star, assuming isotropic luminosity (Israel et al. 2017). However, significant collimation of the disk radiation and strong multi-polar magnetic fields are required to explain the extreme luminosities of ULXs such as NGC 5907 ULX (Israel et al. 2017). The need of a strong magnetic field for the super-Eddington accretion into a neutron star ($> 10^{13} \text{ G}$; see e.g., Israel et al. 2017) comes from the significant reduction in the electron scattering cross section produced for photon energies below the cyclotron energy ($E_c \sim 12 \frac{B}{12\text{G}}$) in the presence of a strong magnetic field. The assumption of isotropic emission in ULXs strongly overestimates the total radiation output, for example Cygnus X-3 seems to be an ULX viewed side-on suffering significant geometrical beaming in our galaxy (Veledina et al. 2024).

Chen et al. (2024) also report the detection of an $H\alpha$ feature showing a shift in the peak emission and where its luminosity follows the periodic undulations of the light curve of SN 2022jli. This variability in the $H\alpha$ feature would be the result of the accretion of hydrogen-rich material from a companion star at periastron encounters as discussed previously. Chen et al. (2024) also report a non-detection of the SN in X-rays placing an upper limit of $2.5 \times 10^{40} \text{ erg s}^{-1}$ in the 30–60 keV energy range at about +230 days from NuSTAR observations, and of $1.32 \times 10^{38} \text{ erg s}^{-1}$ in the 0.5–7 keV energy range at about +260 days from Chandra observations.

The soft X-ray opacity of CC SNe can remain very large for decades, even in SE SNe which are expected to have a factor of 10 lower opacities compared to Type II SNe due to their faster ejecta (Alp et al. 2018). Assuming that the opacity of SN 2022jli is similar to the SNIIB models of Alp et al. (2018), we estimate that at the time of the X-ray observations the opacity at 2 keV, 10 keV and 50 keV are $\sim 30^4$, 10^3 and 40, respectively. Thus all the potential X-ray emission from a central source is absorbed and reprocessed by the SN ejecta, note that the ejecta opacity is larger for the soft X-rays than for more energetic emission. The reprocessing scenario is consistent with the blue optical SN colours, the increase of ejecta temperature during the

re-brightening,¹² and the unusual detection of Mg II lines in the NIR at more than 150 days, implying that the SN emission in the optical and in the NIR bands is from a heated SN ejecta and not direct emission from a central source. At later times (>350 days), the ejecta becomes fully nebular showing strong [O I] lines (Fig. 14).

Following the Chen et al. (2024) super-Eddington hypothesis, King & Lasota (2024) proposed an scenario where the second maximum of SN 2022jli is produced by a highly beamed ULX, with a beaming factor of $b \sim 10^{-3}$ or $b \sim 10^{-4}$ for a $10M_{\odot}$ black-hole or a neutron star, respectively. Additionally, King & Lasota (2024) propose that the second maximum corresponds to an ultra-soft ULX emitting mostly in the UVOIR region of the electromagnetic spectrum. They propose that the orbital plane must be misaligned with respect to the axis of the beamed emission to detect the highly beamed ULX emission and simultaneously observe the shift in the $H\alpha$ emission produced by the orbital motion and accretion from the (low-mass) companion star. The fact that the emission during the second maximum seems to correspond to emission from heated ejecta and not to direct UVOIR emission from an ultra-soft ULX, in addition to the extreme beaming required to explain the high luminosity of SN 2022jli, and the fine tuned geometry to detect both the highly beamed emission from the ULX and the $H\alpha$ periodic variability cast some doubts on the feasibility of scenario proposed by King & Lasota (2024).

4.2. Power injection from a magnetar

Neutron stars are a natural outcome of core-collapse SNe, and they usually possess strong magnetic fields. Pulsars are an example of neutron stars with strong magnetic fields in the range of $B \sim 10^{11} - 10^{13}$ G, and magnetars possess even stronger external magnetic fields in the range of $10^{13} - 10^{15}$ G, with some overlap in their magnetic field strength. The physics associated with the formation of magnetars is poorly understood. The magnetars in our galaxy are characterized by exhibit the most variable neutron star behaviour, emitting high energy electromagnetic radiation mostly in γ -rays ($L_X \sim 5 \times 10^{30} - 10^{36}$ erg s^{-1} ; Kaspi & Beloborodov 2017), and are faint at optical wavelengths. In the case of the formation of a fast spinning neutron star with a strong magnetic field, the rotational spin-down energy of the magnetar can contribute to power the SN light curve. However, the energy injection and the ejecta thermalization process of the magnetar wind are a complex phenomena (see e.g., Kotera et al. 2013; Vurm & Metzger 2021), that can vary with time producing humps, bumps or even periodic undulations in the SN light curves (Vurm & Metzger 2021; Moriya et al. 2022).

Since the discovery of the double-peaked SN 2005bf, the power injection from a magnetar has been recognized as a viable mechanism to produce double-peaked light curves (Maeda et al. 2007). As discussed in Israel et al. (2017) the magnetic field configuration required for the neutron star in NGC 5907 ULX to accrete at a super-Eddington rate is similar to the one envisaged for the so-called magnetars, and as discussed in Medvedev & Poutanen (2013), young pulsars or magnetars can be potential ULXs. Therefore, a natural possibility is that the compact object in SN 2022jli is a magnetar accreting material from a companion star. This is similar to the scenario proposed by Chen et al. (2024), but where a significant fraction of the power supply could come from the magnetar alleviating the need of

super-Eddington accretion to power the second maximum or a privileged viewing angle to an extremely beamed ULX. In this scenario, the accretion at periastron encounters could explain the undulations and the $H\alpha$ periodic variability.

Moriya et al. (2022) studied the effect of variable thermal energy injection in the SN ejecta from a magnetar as the potential cause of bumps in SN light curves. They found that changes in the thermal power injection produced in the SN ejecta from a magnetar can reproduce the light curve bumps such as the ones observed in some SLSNe (e.g., SN 2015bn). One of Moriya et al. (2022) predictions is that an observable consequence of the increase in the power input from a magnetar is an increase in the SN ejecta temperature, in addition to the luminosity increase. The temperature increase should translate in bluer SN colours during the bump, such as the bluer $g - r$ colours observed in SN 2022jli during the maxima of the second bump and the undulations (see Figs. 9 and 10). Their model also predicts a non-noticeable change in the ejecta radius or velocity during the luminosity increase. The latter effect seems to discount a magnetar power supply to explain, for example, the second maximum in the case of SN 2019stc (Moriya et al. 2022).

Potential causes of the change in the thermal energy injection are: i) conversion efficiency, inefficient thermalization at early times (e.g., Kasen et al. 2016); ii) changes in the the fraction of high-energy photons in the pulsar wind nebulae can lead to a change in the thermalization of the energy injected, since the SN ejecta opacity depends on the energy of the photons injected, iii) a change in the angle between the dipole magnetic field and the rotation axis of the neutron star changes the temporal energy injection, and iv) fallback accretion on the magnetar can increase the angular momentum of the neutron star, thus decreasing the magnetar spin period. The angle between the magnetic field axis and the rotation axis of the magnetar determines the spin-down time-scale. If this angle changes periodically the magnetar power injection can suffer a periodic change similar to the one observed in SN 2022jli, however the potential periodic change in the angle could not explain the periodic variation observed in the H I lines.

To explore the magnetar scenario, it is assumed that the second maximum is powered by a magnetar. As discussed in Section 3.2.8, the first maximum of SN 2022jli is consistent with a standard SE SN event with an ejecta mass of about $1.5 M_{\odot}$. Following a methodology similar to the one described in Cartier et al. (2022), and assuming the same ejecta parameters used to fit the first maximum (Section 3.2.8), the second maximum of SN 2022jli is reproduced by the combination of the radioactive decay of $0.12 M_{\odot}$ of ^{56}Ni and the power input from a magnetar (see Fig. 13). We assume full trapping over the period analyzed (no power leakage), with $\kappa = 0.07 \text{ cm}^2 \text{ gr}^{-1}$ and $v_{\text{ej}} = 8500 \text{ km s}^{-1}$, obtaining an initial spin period of $P = 48.5 \text{ ms}$ and a magnetic field of $B = 8.5 \times 10^{14} \text{ G}$. We had to arbitrarily delay the “birth” of the magnetar by 37 days relative to the estimated time of the explosion to reproduce the (pseudo) bolometric light curve of SN 2022jli. In this scenario the late time γ -ray emission reported by Chen et al. (2024) could be interpreted as the emergence of a magnetar wind nebulae (see e.g., Kotera et al. 2013), bringing as a result a drop in the light curve due to leakage of the magnetar power supply. The drop below the luminosity of the radioactive decay chain of $0.12 M_{\odot}$ of ^{56}Ni at +383 requires the escape of significant γ -rays from the radioactive decay of ^{56}Co . The assumption of full trapping and fixed opacity are probably not realistic, but our modelling provides evidence that the secondary maximum could be at least partially, if not completely, powered by a magnetar.

¹² R_{bb} moves inwards during the SN re-brightening (see Fig. 12), a hint of a central heating source.

Recently, Shenar et al. (2023) presented results on the long period binary system (8200 ± 190 d) HD 45166 composed of a main sequence star (class B7 V) and a Wolf-Rayet Helium star with a mass of $\sim 2 M_{\odot}$ and a strong magnetic field. Shenar et al. (2023) estimate that the Helium star will demise as a SE SN, forming an isolated neutron star with a magnetic field of about 1.1×10^{14} G and as spin period $P \leq 40$ ms, similar to the period of the pulsar in the Crab nebula ($P = 33.5$ ms, $B \approx 10^{12}$ G). Shenar et al. (2023) discuss that the Helium star cannot be the result of an evolved $10 M_{\odot}$ or more massive star, instead they propose that the Helium star is the outcome of the merger of two intermediate mass stars (see Shenar et al. 2023, for details). The merger of the two stars may also explain the strong magnetic field detected in the Helium star. A Helium star, potentially similar to the Wolf-Rayet Helium star in HD 45166, with total mass of about $3 M_{\odot}$ and somewhat stronger magnetic field could be the potential progenitor of SN 2022jli in the magnetar scenario.

4.3. Ejecta circum-stellar interaction

The interaction between the SN ejecta and a dense CSM can efficiently transform the kinetic energy of the SN ejecta in thermal energy, powering the SN brightness. This is mechanism behind interacting SLSNe-IIn such as SN 2006gy (Smith et al. 2007), and it has been proposed to explain the large maximum luminosities of SLSNe-Ic (Sorokina et al. 2016; Tolstov et al. 2017a,b). There is evidence that the SN ejecta-CSM interaction may be responsible for the bumps or the light curve undulations observed in some SLSNe after maximum light (Yan et al. 2015, 2017). Some SE SNe such as SN 2014C (Milisavljevic et al. 2015), SN 2017ens (Chen et al. 2018), SN 2017dio (Kuncarayakti et al. 2018), and SN 2018ijp (Tartaglia et al. 2021) interact with abundant hydrogen rich CSM becoming Type IIn SNe. In fact, the presence of dense CSM is a natural consequence of the stellar stripping and bumps are often considered a signature of the ejecta-CSM interaction. The interaction with a dense hydrogen and helium poor CSM is the potential explanation for the double-peaked light curve of the Ic-BL SN 2022xxf (Kuncarayakti et al. 2023).

As discussed in Chen et al. (2024) it is unlikely that the undulations and the light curve of SN 2022jli is powered by ejecta-CSM interaction because the interaction on the rear side would smear any periodic signature from the near side. Additionally, we consider that the spectroscopic evolution of SN 2022jli lack clear signatures of ejecta-CSM interaction, therefore the potential CSM 1) has to be poor in hydrogen and helium, 2) the interaction should occur in a confined region potentially having a low covering fraction such as a dense ring around the progenitor star, and/or 3) the ejecta-CSM interacting region is potentially hidden from the light-of-sight. Finally, as the radiative shock produced by the interaction propagates throughout the dense CSM increasing the optical depth and therefore the photospheric radius at the same time (Moriya et al. 2018) an increase in R_{bb} would be expected. However, SN 2022jli shows the opposite, a decrease in R_{bb} during the SN re-brightening (see Fig. 12). We also consider ejecta-CSM interaction an unlikely scenario to power the second maximum.

5. Summary

We present and analyse observations of the SE SN 2022jli that exhibits a double-peaked light curve, with two maxima separated by about 50 days. After the second maximum the well sampled ZTF and ATLAS light curves reveal periodic undulations

with a period of about 12.5 days (see also Moore et al. 2023; Chen et al. 2024). Using synthetic photometry inferred from spectra obtained during the decline from the first maximum, a host galaxy reddening of $E(B - V)_{\text{host}} = 0.23 \pm 0.06$ was estimated. The SN showed unusually blue $g - r$ colours during its re-brightening, reaching its bluest colour ($g - r \approx -0.45$ mag) at +190 day relative to maximum. We found that in addition to the blue colours the SN shows clear colour variations during its periodic undulations, becoming blue when it is brighter, and it is redder when it is becoming fainter, showing more conspicuous periodic undulations in the bluer bands.

The first maximum of SN 2022jli is consistent with a SN Ic with an estimated expansion velocity of 8500 km s^{-1} , an ejecta mass of $1.5 \pm 0.4 M_{\odot}$ and a radioactive ^{56}Ni mass of $0.12 \pm 0.01 M_{\odot}$. The available photometry seems to show a smooth evolution and does not show undulations during the first maximum, although this cannot be completely discounted due to the sparse coverage in terms of wavelength and sampling of the first maximum. The late optical spectra (>+400 days) confirm the SN Ic nature of SN 2022jli.

We report the detection of relatively weak and broad $H\alpha$ and $\text{Pa}\beta$ double peaked spectral features. The main peak of $H\alpha$ and $\text{Pa}\beta$ features seems to shift following the periodic variation of the light curve undulations, as reported by Chen et al. (2024) for $H\alpha$. We notice that these features become more conspicuous with time, particularly after +100 days. The shift in the $H\text{I}$ spectral features is probably a signature of accretion of hydrogen rich material from a companion star in a binary system. When the spectra of the SN becomes nebular (> +350 days), the hydrogen signatures are not longer detectable in the optical or in the NIR spectra, however a narrow $H\alpha$ emission most likely from the host galaxy is detected at late times.

Using the analytical solutions of Arnett (1982), the second maximum can be modelled as a combination of the ^{56}Ni radioactive decay of $0.12 M_{\odot}$ and the power injection from a magnetar with $P = 48.5$ ms and $B = 8.5 \times 10^{14}$ G with a delayed magnetar “birth” time of 37 days, relative to the estimated time of the explosion. The power injection from a magnetar seems a viable scenario since magnetars are the most variable neutron stars displaying different types of episodic variability (see Mereghetti et al. 2015; Kaspi & Beloborodov 2017). In the magnetar scenario, the late-time γ -ray detection with the Fermi Space Telescope reported by Chen et al. (2024) can be interpreted as the emergence of the magnetar wind nebulae (see e.g., Kotera et al. 2013). The magnetar contributing to power the second maximum of SN 2022jli could fit in the more general picture where magnetars are the power source of SLSNe-Ic, could produce their frequent bumps and undulations, and where pulsars could produce the late time excess observed in some SE SNe (see e.g., Taddia et al. 2016; Ravi et al. 2023).

Alternatively, the second maximum could be produced by the significant accretion of material from the companion star into the compact object left from the explosion (a black-hole or a neutron star), at an extremely large super-Eddington accretion rate ($\sim 10^3$ for a black-hole or $\sim 10^4$ for a neutron star) or could be an ULX displaying extremely beamed emission ($b \sim 10^{-3}$ or 10^{-4}) viewed just at the right angle as proposed by King & Lasota (2024).

From +190 days until about +224 days unambiguous 1st CO overtone emission is detected in the NIR spectra of SN 2022jli. At later times (>+385 days), the 1st CO overtone is not longer detected. From about +200 days a strong infrared excess is detected in the NIR photometry of SN 2022jli, which is particularly strong in the K_s -band. Later NIR observations (> +385 days)

demonstrate that this infrared excess is produced by thermal emission from hot dust, with a temperature of 900–650 K. Depending on the assumptions of the dust composition, the estimated dust mass is $2 - 16 \times 10^{-4} M_{\odot}$. This emission could be either produced by a strong IR echo from pre-existing dust surrounding the SN, or from newly formed dust in the SN ejecta. The detection of CO and of dust potentially formed in the ejecta of SN 2022jli, are important to understand the formation of molecules and dust formation in the ejecta of SE SNe. At more than +800 days the SN is still bright at infrared wavelengths (priv. communication), therefore infrared observations with *JWST* should complement the observations presented here providing an unprecedented view of the molecule and dust emission in SN 2022jli over several years, or even in a decade long time scale.

Acknowledgements. R.C. acknowledges support from Gemini ANID ASTRO21-0036. M.D.S. is funded by the Independent Research Fund Denmark (IRFD, grant number 10.46540/2032-00022B). Based on observations obtained at the international Gemini Observatory under proposals GS-2022A-Q-415, GS-2022B-Q-407 and GS-2022B-FT-206 (PI R. Cartier), a program of NSF's NOIRLab, which is managed by the Association of Universities for Research in Astronomy (AURA) under a cooperative agreement with the National Science Foundation on behalf of the Gemini Observatory partnership: the National Science Foundation (United States), National Research Council (Canada), Agencia Nacional de Investigación y Desarrollo (Chile), Ministerio de Ciencia, Tecnología e Innovación (Argentina), Ministério da Ciência, Tecnologia, Inovações e Comunicações (Brazil), and Korea Astronomy and Space Science Institute (Republic of Korea). Also based on observations obtained at the Southern Astrophysical Research (SOAR) telescope, which is a joint project of the Ministério da Ciência, Tecnologia e Inovações (MCTI/LNA) do Brasil, the US National Science Foundation's NOIRLab, the University of North Carolina at Chapel Hill (UNC), and Michigan State University (MSU). Based on observations collected at the European Southern Observatory under ESO programmes 382.B-0331(A) and 108.220C.014.

This research has made use of the NASA/IPAC Extragalactic Database (NED), which is operated by the Jet Propulsion Laboratory, California Institute of Technology, under contract with the National Aeronautics and Space Administration. This work has also made use of data from the Asteroid Terrestrial-impact Last Alert System (ATLAS) project. The Asteroid Terrestrial-impact Last Alert System (ATLAS) project is primarily funded to search for near earth asteroids through NASA grants NN12AR55G, 80NSSC18K0284, and 80NSSC18K1575; byproducts of the NEO search include images and catalogs from the survey area. This work was partially funded by Kepler/K2 grant J1944/80NSSC19K0112 and HST GO-15889, and STFC grants ST/T000198/1 and ST/S006109/1. The ATLAS science products have been made possible through the contributions of the University of Hawaii Institute for Astronomy, the Queen's University Belfast, the Space Telescope Science Institute, the South African Astronomical Observatory, and The Millennium Institute of Astrophysics (MAS), Chile. This publication makes use of data products from the Wide-field Infrared Survey Explorer, which is a joint project of the University of California, Los Angeles, and the Jet Propulsion Laboratory/California Institute of Technology, funded by the National Aeronautics and Space Administration. This work has made use of data from the European Space Agency (ESA) mission *Gaia* (<https://www.cosmos.esa.int/gaia>), processed by the *Gaia* Data Processing and Analysis Consortium (DPAC, <https://www.cosmos.esa.int/web/gaia/dpac/consortium>). Funding for the DPAC has been provided by national institutions, in particular the institutions participating in the *Gaia* Multilateral Agreement.

Appendix A: Synthetic photometry

In Table A.1 is presented the synthetic photometry performed to LDSS-3 and EFOSC2 spectra obtained on May 22nd and 24th, 2022, respectively.

Table A.1. Summary of synthetic photometry for SN 2022jli.

Template spectrum	MJD phot (days)	Scaling band	Scaling phot. (mag)	g_{ZTF} (mag)	r_{ZTF} (mag)	c_{ATLAS} (mag)	o_{ATLAS} (mag)	G (mag)	Clear (mag)
LDSS-3_22-05-2022	59721.4	<i>i</i> band	14.444(0.029)	15.82(0.10)	14.71(0.10)	15.28(0.10)	14.59(0.10)	14.84(0.10)	14.57(0.10)
EFOSC2_24-05-2022	59723.4	<i>V</i> band	15.217(0.017)	15.95(0.10)	14.86(0.10)	15.40(0.10)	14.72(0.10)	14.94(0.10)	14.61(0.10)

Appendix B: Pseudo-bolometric light curves

To construct the pseudo-bolometric light curve of SN 2022jli we followed the approach of constructing optical spectral templates. During the first and on the rise to the secondary maxima a few epochs of multi-band photometry are available, therefore we used the optical spectra of SN 2022jli that provided the shape of the spectral energy distribution (SED) of the SN. The spectra of SN 2022jli were scaled using optical photometry obtained as close in time to the spectra as possible. These spectrophotometric templates were integrated to derive the total luminosity emitted by SN 2022jli in the optical regime (3800 – 9000 Å). When no spectra of SN 2022jli are available, for example at maximum, we used the optical spectra of SN 2013ge, which shows a SED and spectral features similar to SN 2022jli during the normal Ic phase of SN 2022jli, around maximum light. The spectra of SN 2013ge were colour matched to the SN optical photometry of SN 2013ge, dereddened using the reddening in the line-of-sight to SN 2013ge ($E(B - V) = 0.067$; Drout et al. 2016), and then the spectral template was reddened using the total color excess in the direction of SN 2022jli (i.e., $E(B - V)_{\text{tot}} = 0.27$ mag; see Section 3.2.3). Finally, the spectral template was scaled using Gaia photometry of SN 2022jli close to maximum light.

We have identified three sources of potential systematic errors in using spectral templates to derive bolometric light curves. The first source is a poor calibration of the spectrum due to slit losses or poor flux calibration. When multi-band photometry is available this can be solved by matching the SN colours of the spectra to the photometry as described in Cartier et al. (2022). This colour-matching procedure was applied to the spectra templates of SN 2013ge, and correspond to minimal corrections. We have found comparing synthetic photometry with actual observations that this effect is usually small (<5%), however conservatively we will assume 10% uncertainty for spectra that have been scaled and not colour-matched to multi-band photometry. The second potential source of systematic error is using a spectral template from a substitute object, as is the case of SN 2013ge at maximum light. Given the similarity between SN 2022jli at +12 days and SN 2013ge at +7 days, to quantify this effect we used the spectral template of SN 2013ge at +7 days to compute the bolometric luminosity of SN 2022jli at +12 days, instead of the actual spectrum. This procedure shows that the use of a substitute object as spectral template, having a similar spectral shape, it can introduce a systematic error of the order of $\approx 13\%$ in the computation of the bolometric luminosity.

Finally, we evaluate the effect of using a spectral template from a different phase, for example, this can be the case of using a spectral template obtained at the time of V -band maximum to estimate the luminosity at the i -band maximum, even though both are close in time, the shape of the spectra is different at both epochs introducing a systematic error. We estimate this effect by comparing the pseudo-bolometric luminosity obtained for SN 2022jli at maximum, from using the spectral templates of SN 2013ge at +1 days and at +7 days relative to the B -band maximum. We find that this can introduce a systematic difference of $\approx 10\%$ in the pseudo-bolometric optical luminosity. We add in quadrature all these uncertainties in addition to the actual median of the errors from the photometry used to scale and colour match the spectra.

References

Alp, D., Larsson, J., Fransson, C., et al. 2018, *ApJ*, 864, 175
 Anderson, J. P. 2019, *A&A*, 628, A7
 Angus, C. R., Smith, M., Sullivan, M., et al. 2019, *MNRAS*, 487, 2215

Anupama, G. C., Sahu, D. K., Deng, J., et al. 2005, *ApJ*, 631, L125
 Arnett, W. D. 1982, *ApJ*, 253, 785
 Balcon, C. 2022, *Transient Name Server Classification Report*, 2022-3048, 1
 Banerjee, D. P. K., Joshi, V., Evans, A., et al. 2018, *MNRAS*, 481, 806
 Becker, A. 2015, *HOTPANTS: High Order Transform of PSF ANd Template Subtraction*, Astrophysics Source Code Library, record ascl:1504.004
 Bellm, E. C., Kulkarni, S. R., Graham, M. J., et al. 2019, *PASP*, 131, 018002
 Bersten, M. C., Benvenuto, O., & Hamuy, M. 2011, *ApJ*, 729, 61
 Bersten, M. C., Benvenuto, O. G., Nomoto, K., et al. 2012, *ApJ*, 757, 31
 Bouchet, P., Phillips, M. M., Suntzeff, N. B., et al. 1991, *A&A*, 245, 490
 Buzzoni, B., Delabre, B., Dekker, H., et al. 1984, *The Messenger*, 38, 9
 Cano, Z. 2013, *MNRAS*, 434, 1098
 Cartier, R., Hamuy, M., Contreras, C., et al. 2022, *MNRAS*, 514, 2627
 Cartier, R., Rho, J., Hoeflich, P., et al. 2021, *The Astronomer's Telegram*, 14653, 1
 Catchpole, R. M., Whitelock, P. A., Feast, M. W., et al. 1988, *MNRAS*, 231, 75P
 Chatzopoulos, E., Wheeler, J. C., Vinko, J., Horvath, Z. L., & Nagy, A. 2013, *ApJ*, 773, 76
 Chen, P., Gal-Yam, A., Sollerman, J., et al. 2024, *Nature*, 625, 253
 Chen, T. W., Inserra, C., Fraser, M., et al. 2018, *ApJ*, 867, L31
 Clemens, J. C., Crain, J. A., & Anderson, R. 2004, in *Society of Photo-Optical Instrumentation Engineers (SPIE) Conference Series*, Vol. 5492, *Ground-based Instrumentation for Astronomy*, ed. A. F. M. Moorwood & M. Iye, 331–340
 Conti, P. S. 1975, *Memoires of the Societe Royale des Sciences de Liege*, 9, 193
 Cosentino, S. P., Evans, C. R., Inserra, C., et al. 2022, *Transient Name Server Classification Report*, 2022-1409, 1
 Cushing, M. C., Vacca, W. D., & Rayner, J. T. 2004, *PASP*, 116, 362
 Dalton, G. B., Caldwell, M., Ward, A. K., et al. 2006, in *Society of Photo-Optical Instrumentation Engineers (SPIE) Conference Series*, Vol. 6269, *Ground-based and Airborne Instrumentation for Astronomy*, ed. I. S. McLean & M. Iye, 62690X
 De Cia, A., Gal-Yam, A., Rubin, A., et al. 2018, *ApJ*, 860, 100
 Dessart, L., Hillier, D. J., Woosley, S., et al. 2015, *MNRAS*, 453, 2189
 Dessart, L., Yoon, S.-C., Aguilera-Dena, D. R., & Langer, N. 2020, *A&A*, 642, A106
 Dong, Y., Valenti, S., Ashall, C., et al. 2023, *arXiv e-prints*, arXiv:2309.09433
 Draine, B. T. 2016, *ApJ*, 831, 109
 Draine, B. T. & Lee, H. M. 1984, *ApJ*, 285, 89
 Drout, M. R., Milisavljevic, D., Parrent, J., et al. 2016, *ApJ*, 821, 57
 Drout, M. R., Soderberg, A. M., Gal-Yam, A., et al. 2011, *ApJ*, 741, 97
 Eikenberry, S., Bandyopadhyay, R., Bennett, J. G., et al. 2012, in *Proc. SPIE*, Vol. 8446, *Ground-based and Airborne Instrumentation for Astronomy IV*, 84460I
 Eikenberry, S. S., Elston, R., Raines, S. N., et al. 2004, in *Proc. SPIE*, Vol. 5492, *Ground-based Instrumentation for Astronomy*, ed. A. F. M. Moorwood & M. Iye, 1196–1207
 Elias, J. H., Gregory, B., Phillips, M. M., et al. 1988, *ApJ*, 331, L9
 Emerson, J., McPherson, A., & Sutherland, W. 2006, *The Messenger*, 126, 41
 Ergon, M., Jerkstrand, A., Sollerman, J., et al. 2015, *A&A*, 580, A142
 Ergon, M., Sollerman, J., Fraser, M., et al. 2014, *A&A*, 562, A17
 Fang, Q., Maeda, K., Kuncarayakti, H., et al. 2022, *ApJ*, 928, 151
 Filippenko, A. V. 1997, *ARA&A*, 35, 309
 Fitzpatrick, E. L. 1999, *PASP*, 111, 63
 Folatelli, G., Contreras, C., Phillips, M. M., et al. 2006, *ApJ*, 641, 1039
 Gaia Collaboration, Prusti, T., de Bruijne, J. H. J., et al. 2016, *A&A*, 595, A1
 Gal-Yam, A. 2017, in *Handbook of Supernovae*, ed. A. W. Alsabti & P. Murdin, 195
 Gerardy, C. L., Fesen, R. A., Nomoto, K., et al. 2002, *PASJ*, 54, 905
 Gimeno, G., Roth, K., Chiboucas, K., et al. 2016, in *Society of Photo-Optical Instrumentation Engineers (SPIE) Conference Series*, Vol. 9908, *Ground-based and Airborne Instrumentation for Astronomy VI*, ed. C. J. Evans, L. Simard, & H. Takami, 99082S
 Gomez, S., Berger, E., Hosseinzadeh, G., et al. 2021, *ApJ*, 913, 143
 Grzegorzec, J. 2022, *Transient Name Server Classification Report*, 2022-1261, 1
 Gutiérrez, C. P., Bersten, M. C., Orellana, M., et al. 2021, *MNRAS*, 504, 4907
 Gutiérrez, C. P., Pastorello, A., Bersten, M., et al. 2022, *MNRAS*, 517, 2056
 Hamuy, M., Folatelli, G., Morrell, N. I., et al. 2006, *PASP*, 118, 2
 Hirai, R. & Podsiadlowski, P. 2022, *MNRAS*, 517, 4544
 Holmbo, S., Stritzinger, M. D., Karamahmetoglu, E., et al. 2023, *A&A*, 675, A83
 Hook, I. M., Jørgensen, I., Allington-Smith, J. R., et al. 2004, *PASP*, 116, 425
 Hosseinzadeh, G., Berger, E., Metzger, B. D., et al. 2022, *ApJ*, 933, 14
 Hueichapan, E. D., Contreras, C., Cartier, R., et al. 2022, *MNRAS*, 513, 2965
 Hunter, D. J., Valenti, S., Kotak, R., et al. 2009, *A&A*, 508, 371
 Inserra, C., Smartt, S. J., Jerkstrand, A., et al. 2013, *ApJ*, 770, 128
 Israel, G. L., Belfiore, A., Stella, L., et al. 2017, *Science*, 355, 817
 Itagaki, K. 2022, *Transient Name Server Discovery Report*, 2022-3014, 1
 Kaaret, P., Feng, H., & Roberts, T. P. 2017, *ARA&A*, 55, 303
 Kasen, D. 2010, *ApJ*, 708, 1025

- Kasen, D. & Bildsten, L. 2010, *ApJ*, 717, 245
- Kasen, D., Metzger, B. D., & Bildsten, L. 2016, *ApJ*, 821, 36
- Kaspi, V. M. & Beloborodov, A. M. 2017, *ARA&A*, 55, 261
- Khatami, D. K. & Kasen, D. N. 2019, *ApJ*, 878, 56
- King, A. & Lasota, J.-P. 2024, arXiv e-prints, arXiv:2402.09509
- Kotak, R., Meikle, P., Pozzo, M., et al. 2006, *ApJ*, 651, L117
- Kotak, R., Meikle, P., van Dyk, S. D., Höflich, P. A., & Mattila, S. 2005, *ApJ*, 628, L123
- Kotak, R., Meikle, W. P. S., Farrah, D., et al. 2009, *ApJ*, 704, 306
- Kotera, K., Phinney, E. S., & Olinto, A. V. 2013, *MNRAS*, 432, 3228
- Krisciunas, K., Contreras, C., Burns, C. R., et al. 2017, *AJ*, 154, 211
- Kuncarayakti, H., Maeda, K., Ashall, C. J., et al. 2018, *ApJ*, 854, L14
- Kuncarayakti, H., Sollerman, J., Izzo, L., et al. 2023, arXiv e-prints, arXiv:2303.16925
- Lang, D., Hogg, D. W., Mierle, K., Blanton, M., & Roweis, S. 2010, *AJ*, 139, 1782
- Laor, A. & Draine, B. T. 1993, *ApJ*, 402, 441
- Leloudas, G., Chatzopoulos, E., Dilday, B., et al. 2012, *A&A*, 541, A129
- Liljegren, S., Jerkstrand, A., & Gruner, J. 2020, *A&A*, 642, A135
- Lunnan, R., Chornock, R., Berger, E., et al. 2018, *ApJ*, 852, 81
- Lyman, J. D., Bersier, D., James, P. A., et al. 2016, *MNRAS*, 457, 328
- Maeda, K., Kawabata, K., Mazzali, P. A., et al. 2008, *Science*, 319, 1220
- Maeda, K., Tanaka, M., Nomoto, K., et al. 2007, *ApJ*, 666, 1069
- Mainzer, A., Bauer, J., Cutri, R. M., et al. 2014, *ApJ*, 792, 30
- Mainzer, A., Grav, T., Bauer, J., et al. 2011, *ApJ*, 743, 156
- Medvedev, A. S. & Poutanen, J. 2013, *MNRAS*, 431, 2690
- Meikle, W. P. S., Allen, D. A., Spyromilio, J., & Varani, G. F. 1989, *MNRAS*, 238, 193
- Mereghetti, S., Pons, J. A., & Melatos, A. 2015, *Space Sci. Rev.*, 191, 315
- Milislavjevic, D., Margutti, R., Kamble, A., et al. 2015, *ApJ*, 815, 120
- Milne, P. A., The, L. S., & Leising, M. D. 1999, *ApJS*, 124, 503
- Monard, L. 2022, *Transient Name Server Discovery Report*, 2022-1198, 1
- Monard, L. A. G., Moore, M., & Li, W. 2005, *IAU Circ.*, 8507, 1
- Moore, T., Smartt, S. J., Nicholl, M., et al. 2023, *ApJ*, 956, L31
- Moriya, T. J., Murase, K., Kashiyama, K., & Blinnikov, S. I. 2022, *MNRAS*, 513, 6210
- Moriya, T. J., Sorokina, E. I., & Chevalier, R. A. 2018, *Space Sci. Rev.*, 214, 59
- Mould, J. R., Huchra, J. P., Freedman, W. L., et al. 2000, *ApJ*, 529, 786
- Nicholl, M., Berger, E., Margutti, R., et al. 2016a, *ApJ*, 828, L18
- Nicholl, M., Berger, E., Smartt, S. J., et al. 2016b, *ApJ*, 826, 39
- Nicholl, M. & Smartt, S. J. 2016, *MNRAS*, 457, L79
- Nicholl, M., Smartt, S. J., Jerkstrand, A., et al. 2015, *ApJ*, 807, L18
- Orellana, M. & Bersten, M. 2022, arXiv e-prints, arXiv:2209.03923
- Phillips, M. M., Simon, J. D., Morrell, N., et al. 2013, *ApJ*, 779, 38
- Piro, A. L. 2015, *ApJ*, 808, L51
- Piro, A. L., Haynie, A., & Yao, Y. 2021, *ApJ*, 909, 209
- Podsiadlowski, P., Joss, P. C., & Hsu, J. J. L. 1992, *ApJ*, 391, 246
- Poznanski, D., Prochaska, J. X., & Bloom, J. S. 2012, *MNRAS*, 426, 1465
- Prentice, S. J., Maguire, K., Siebenaler, L., & Jerkstrand, A. 2022, *MNRAS*, 514, 5686
- Prentice, S. J., Mazzali, P. A., Pian, E., et al. 2016, *MNRAS*, 458, 2973
- Ravi, A. P., Rho, J., Park, S., et al. 2023, *ApJ*, 950, 14
- Rho, J., Evans, A., Geballe, T. R., et al. 2021, *ApJ*, 908, 232
- Rho, J., Geballe, T. R., Banerjee, D. P. K., et al. 2018, *ApJ*, 864, L20
- Richmond, M. W., Treffers, R. R., Filippenko, A. V., et al. 1994, *AJ*, 107, 1022
- Ryder, S. D., Zasov, A. V., McIntyre, V. J., Walsh, W., & Sil'chenko, O. K. 1998, *MNRAS*, 293, 411
- Sana, H., de Mink, S. E., de Koter, A., et al. 2012, *Science*, 337, 444
- Schlafly, E. F. & Finkbeiner, D. P. 2011, *ApJ*, 737, 103
- Schlawin, E., Herter, T. L., Henderson, C., et al. 2014, in *Society of Photo-Optical Instrumentation Engineers (SPIE) Conference Series*, Vol. 9147, *Ground-based and Airborne Instrumentation for Astronomy V*, ed. S. K. Ramsay, I. S. McLean, & H. Takami, 91472H
- Schlegel, D. J., Finkbeiner, D. P., & Davis, M. 1998, *ApJ*, 500, 525
- Shahbandeh, M., Hsiao, E. Y., Ashall, C., et al. 2022, *ApJ*, 925, 175
- Shahbandeh, M., Sarangi, A., Temim, T., et al. 2023, *MNRAS*, 523, 6048
- Shappee, B. J., Prieto, J. L., Grupe, D., et al. 2014, *ApJ*, 788, 48
- Shenar, T., Wade, G. A., Marchant, P., et al. 2023, *Science*, 381, 761
- Shivvers, I., Filippenko, A. V., Silverman, J. M., et al. 2019, *MNRAS*, 482, 1545
- Smartt, S. J., Valenti, S., Fraser, M., et al. 2015, *A&A*, 579, A40
- Smith, K. W., Smartt, S. J., Young, D. R., et al. 2020, *PASP*, 132, 085002
- Smith, M., Sullivan, M., D'Andrea, C. B., et al. 2016, *ApJ*, 818, L8
- Smith, N., Li, W., Foley, R. J., et al. 2007, *ApJ*, 666, 1116
- Snodgrass, C., Saviane, I., Monaco, L., & Sinclair, P. 2008, *The Messenger*, 132, 18
- Sorokina, E., Blinnikov, S., Nomoto, K., Quimby, R., & Tolstov, A. 2016, *ApJ*, 829, 17
- Springob, C. M., Haynes, M. P., Giovanelli, R., & Kent, B. R. 2005, *ApJS*, 160, 149
- Spyromilio, J., Meikle, W. P. S., Learner, R. C. M., & Allen, D. A. 1988, *Nature*, 334, 327
- Stritzinger, M., Mazzali, P., Phillips, M. M., et al. 2009, *ApJ*, 696, 713
- Stritzinger, M., Taddia, F., Fransson, C., et al. 2012, *ApJ*, 756, 173
- Stritzinger, M. D., Anderson, J. P., Contreras, C., et al. 2018a, *A&A*, 609, A134
- Stritzinger, M. D., Baron, E., Taddia, F., et al. 2024, *A&A*, 686, A79
- Stritzinger, M. D., Holmbo, S., Morrell, N., et al. 2023, *A&A*, 675, A82
- Stritzinger, M. D., Taddia, F., Burns, C. R., et al. 2018b, *A&A*, 609, A135
- Szalai, T., Vinkó, J., Balog, Z., et al. 2011, *A&A*, 527, A61
- Taddia, F., Fremling, C., Sollerman, J., et al. 2016, *A&A*, 592, A89
- Taddia, F., Sollerman, J., Fremling, C., et al. 2018a, *A&A*, 609, A106
- Taddia, F., Sollerman, J., Leloudas, G., et al. 2015, *A&A*, 574, A60
- Taddia, F., Stritzinger, M. D., Bersten, M., et al. 2018b, *A&A*, 609, A136
- Tartaglia, L., Sollerman, J., Barbarino, C., et al. 2021, *A&A*, 650, A174
- Taubenberger, S., Valenti, S., Benetti, S., et al. 2009, *MNRAS*, 397, 677
- Tinyanont, S., Foley, R. J., Taggart, K., et al. 2024, *PASP*, 136, 014201
- Tinyanont, S., Kasliwal, M. M., Krafton, K., et al. 2019, *ApJ*, 873, 127
- Tolstov, A., Nomoto, K., Blinnikov, S., et al. 2017a, *ApJ*, 835, 266
- Tolstov, A., Zhiglo, A., Nomoto, K., et al. 2017b, *ApJ*, 845, L2
- Tominaga, N., Tanaka, M., Nomoto, K., et al. 2005, *ApJ*, 633, L97
- Tonry, J. L., Denneau, L., Heinze, A. N., et al. 2018, *PASP*, 130, 064505
- Vacca, W. D., Cushing, M. C., & Rayner, J. T. 2003, *PASP*, 115, 389
- van Dokkum, P. G. 2001, *PASP*, 113, 1420
- Veledina, A., Muleri, F., Poutanen, J., et al. 2024, *Nature Astronomy* [arXiv:2303.01174]
- Vurm, I. & Metzger, B. D. 2021, *ApJ*, 917, 77
- Woosley, S. E. 2010, *ApJ*, 719, L204
- Wright, E. L., Eisenhardt, P. R. M., Mainzer, A. K., et al. 2010, *AJ*, 140, 1868
- Yan, L., Lunnan, R., Perley, D. A., et al. 2017, *ApJ*, 848, 6
- Yan, L., Quimby, R., Ofek, E., et al. 2015, *ApJ*, 814, 108
- Yoon, S.-C. 2017, *MNRAS*, 470, 3970